



1 EMDNA: Ensemble Meteorological Dataset for North America

2 Guoqiang Tang^{1,2}, Martyn P. Clark^{1,2}, Simon Michael Papalexiou^{2,3}, Andrew J. Newman⁴, Andrew
3 W. Wood⁴, Dominique Brunet⁵, Paul H. Whitfield^{1,2}

4

5 ¹University of Saskatchewan Coldwater Lab, Canmore, Alberta, Canada

6 ²Centre for Hydrology, University of Saskatchewan, Saskatoon, Saskatchewan, Canada

7 ³Department of Civil, Geological and Environmental Engineering, University of Saskatchewan, Saskatchewan,
8 Canada

9 ⁴National Center for Atmospheric Research, Boulder, Colorado

10 ⁵Meteorological Research Division, Environment and Climate Change Canada, Toronto, Ontario, Canada

11

12 **Abstract:** Probabilistic methods are very useful to estimate the spatial variability in meteorological conditions (e.g.,
13 spatial patterns of precipitation and temperature across large domains). In ensemble probabilistic methods, “equally
14 plausible” ensemble members are used to approximate the probability distribution, hence uncertainty, of a spatially
15 distributed meteorological variable conditioned on the available information. The ensemble can be used to evaluate
16 the impact of the uncertainties in a myriad of applications. This study develops the Ensemble Meteorological Dataset
17 for North America (EMDNA). EMDNA has 100 members with daily precipitation amount, mean daily temperature,
18 and daily temperature range at 0.1° spatial resolution from 1979 to 2018, derived from a fusion of station observations
19 and reanalysis model outputs. The station data used in EMDNA are from a serially complete dataset for North America
20 (SCDNA) that fills gaps in precipitation and temperature measurements using multiple strategies. Outputs from three
21 reanalysis products are regridded, corrected, and merged using the Bayesian Model Averaging. Optimal Interpolation
22 (OI) is used to merge station- and reanalysis-based estimates. EMDNA estimates are generated based on OI estimates
23 and spatiotemporally correlated random fields. Evaluation results show that (1) the merged reanalysis estimates
24 outperform raw reanalysis estimates, particularly in high latitudes and mountainous regions; (2) the OI estimates are
25 more accurate than the reanalysis and station-based regression estimates, with the most notable improvement for
26 precipitation occurring in sparsely gauged regions; and (3) EMDNA estimates exhibit good performance according to
27 the diagrams and metrics used for probabilistic evaluation. We also discuss the limitations of the current framework
28 and highlight that persistent efforts are needed to further develop probabilistic methods and ensemble datasets. Overall,
29 EMDNA is expected to be useful for hydrological and meteorological applications in North America. The whole
30 dataset and a teaser dataset (a small subset of EMDNA for easy download and preview) are available at
31 <https://doi.org/10.20383/101.0275> (Tang et al., 2020a).



32 1. Introduction

33 Precipitation and temperature data are fundamental inputs for a wide variety of geoscientific and operational
34 applications benefitting society (Eischeid et al., 2000; Trenberth et al., 2003; Wu et al., 2014; Yin et al., 2018).
35 Accurately estimating spatial meteorological fields is still challenging despite the availability of many measurement
36 approaches (e.g., meteorological stations, weather radars, and satellite sensors) and atmospheric models (Kirstetter et
37 al., 2015; Sun et al., 2018; Hu et al., 2019; Newman et al., 2019a). There is consequently substantial uncertainty in
38 analyses of spatially distributed meteorological variables.

39 The uncertainty in spatial meteorological estimates depends on both the measurements available and the climate of
40 the region of study. Whilst meteorological stations provide the most reliable observations at the point scale, spatial
41 meteorological estimates based on station data can be degraded by the sparsity of station networks in remote regions
42 and by measurement errors caused by factors such as evaporation/wetting loss and under-catch of precipitation (Sevruk,
43 1984; Goodison et al., 1998; Nešpor and Sevruk, 1999; Yang et al., 2005; Scaff et al., 2015; Kochendorfer et al., 2018).
44 Interpolating station data to a regular grid can introduce additional uncertainties due to factors such as method choices
45 and topographic variations. The accuracy of precipitation estimated from ground radars is affected by factors such as
46 beam blockage, signal attenuation, ground clutter, and uncertainties in the reflectivity-rainfall relationships (Dinku et
47 al., 2002; Kirstetter et al., 2015). Moreover, the spatial and temporal coverage of ground radars is limited to large
48 populated areas in most regions of the world. Satellite sensors provide quasi-global estimates of meteorological
49 variables, but their utility can be limited by short sampling periods with insufficient coverage and return frequency,
50 indirect measurements, imperfect retrieval algorithms, and instrument limitations (Adler et al., 2017; Tang et al., 2016,
51 2020b). Reanalysis models, which provide long-term global simulations, also contain biases and uncertainties caused
52 by the imperfect model representations of physical processes, observational constraints, model resolution, and model
53 parameterization (Donat et al., 2014; Parker, 2016).

54 In recent years, numerous deterministic gridded precipitation and temperature datasets based on observed or simulated
55 data from single or multiple sources have become available to the public (Maurer et al., 2002; Huffman et al., 2007;
56 Mahfouf et al., 2007; Daly et al., 2008; Di Luzio et al., 2008; Haylock et al., 2008; Livneh et al., 2013; Weedon et al.,
57 2014; Fick and Hijmans, 2017; Beck et al., 2019; Ma et al., 2020; Harris et al., 2020). Since the uncertainties vary in
58 space and time, deterministic products do not always agree with each other (Donat et al., 2014; Henn et al., 2018; Sun
59 et al., 2018; Newman et al., 2019a; Tang et al., 2020b). The uncertainties can be propagated to applications such as
60 hydrological modeling and climate analysis (Clark et al., 2006; Hong et al., 2006; Slater and Clark, 2006; Mears et
61 al., 2011; Rodell et al., 2015; Aalto et al., 2016). Proper understanding of the uncertainties can benefit the objective
62 application of meteorological analyses and further improve existing products, yet few gridded datasets provide such
63 uncertainty estimates (Cornes et al., 2018; Frei and Isotta, 2019).

64 Probabilistic datasets now can provide alternatives to deterministic datasets for quantitative precipitation and
65 temperature estimation and have advantages in estimating uncertainties and representing extremes (Kirstetter et al.,



66 2015; Mendoza et al., 2017; Frei and Isotta, 2019). Recently, several ensemble meteorological datasets have become
67 available. For example, Morice et al. (2012) develop the observation-based HadCRUT4 global temperature datasets
68 with 100 members. Caillouet et al. (2019) develop the Spatially COherent Probabilistic Extended Climate dataset
69 (SCOPE Climate) with 25 members in France. Newman et al. (2015, 2019b, 2020) continually extend the probabilistic
70 estimation methodology proposed by Clark and Slater (2006), and produce ensemble precipitation and temperature
71 datasets in the contiguous USA (CONUS), the Hawaii Islands, and Alaska and Yukon, respectively. Moreover, several
72 widely used deterministic datasets now have ensemble versions in view of the advantages of probabilistic estimates.
73 Cornes et al. (2018) developed the ensemble version (100 members) of the Haylock et al. (2008) Europe-wide E-OBS
74 temperature and precipitation datasets. Khedhaouiria et al. (2020) developed the experimental High-Resolution
75 Ensemble Precipitation Analysis (HREPA) for Canada and the northern part of the CONUS with 24 members, which
76 can be regarded as an experimental ensemble version of the Canadian Precipitation Analysis (CaPA; Mahfouf et al.,
77 2007; Fortin et al., 2015).

78 Our objective is to develop an Ensemble Meteorological Dataset for North America (EMDNA) from 1979 to 2018.
79 To improve the quality of estimates in sparsely gauged regions, station data and reanalysis outputs are merged to
80 generate gridded precipitation and temperature estimates. Then, ensemble estimates are produced using the
81 probabilistic method described by Clark and Slater (2006) and Newman et al. (2015, 2019b, 2020). EMDNA has 100
82 members and contains daily precipitation amount, mean daily temperature (T_{mean}), and daily temperature range
83 (T_{range}) at 0.1° spatial resolution. Minimum and maximum temperature can be calculated from T_{mean} and T_{range} .
84 It is expected that the EMDNA will be useful for a variety of applications in North America.

85 **2. Datasets**

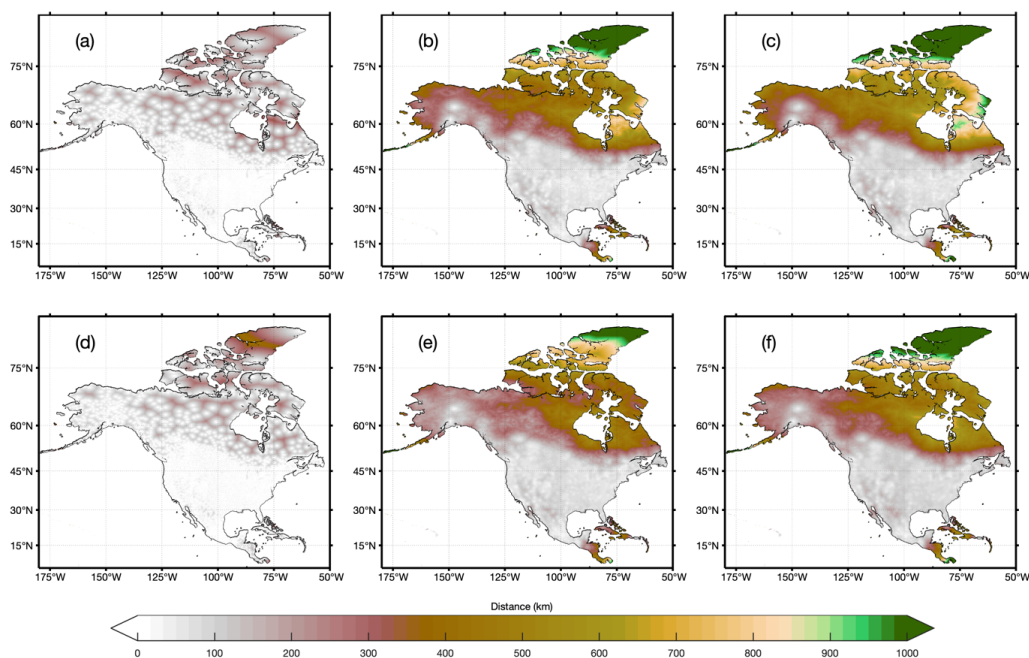
86 Station observations often have missing values and short record lengths (Kemp et al., 1983). This study uses station
87 precipitation and minimum/maximum temperature data from the Serially Complete Dataset for North America (Tang
88 et al., 2020c), which is open-access on Zenodo (<https://doi.org/10.5281/zenodo.3735533>; Access Date: July 25, 2020).
89 T_{mean} and T_{range} are calculated from minimum and maximum temperature data. In SCDNA, raw measurements
90 undergo strict quality control checks, and data gaps are filled by combining estimates from multiple strategies.
91 SCDNA covers the period from 1979 to 2018 and has 24615 precipitation stations and 19579 temperature stations.

92 Station-based gridded meteorological estimates usually rely on a certain number of neighboring stations surrounding
93 the target location. For most regions in CONUS, the search radius to find 20 or 30 neighboring stations (lower and
94 upper limits for station-based gridded estimates in Sect. 3.1) is smaller than 100 km (Fig. 1). For the regions northern
95 to 50°N or southern to 20°N , however, the search radius is much larger and even exceeds 1000 km in the Arctic
96 Archipelago. The sparse station network at higher latitudes motivates our decision to optimally combine station data
97 with reanalysis products.



98 The reanalysis products used in this study include the fifth generation of European Centre for Medium-Range Weather
99 Forecasts (ECMWF) atmospheric reanalyses of the global climate (ERA5; Hersbach et al., 2020), the Modern-Era
100 Retrospective analysis for Research and Applications, Version 2 (MERRA-2; Gelaro et al., 2017), and the Japanese
101 55-year Reanalysis (JRA-55; Kobayashi et al., 2015). The spatial resolutions of ERA5, MERRA-2, and JRA-55 are
102 $0.25^{\circ} \times 0.25^{\circ}$, $0.5^{\circ} \times 0.625^{\circ}$, and ~ 55 km, respectively. Their start years are 1979, 1980, and 1958, respectively.
103 Therefore, only ERA5 and JRA-55 are used for 1979 throughout this study. Although reanalysis models assimilate
104 observations from various sources, they differ with station measurements in many aspects (Parker, 2016) and often
105 contain large uncertainties as shown by assessment and multi-source merging studies (e.g., Donat et al., 2014; Lader
106 et al., 2016; Beck et al., 2017, 2019; Tang et al., 2020b). Thereby, the possible dependence between reanalysis
107 estimates and station data is not considered when merging them in this study.

108 The elevation data are sourced from the 3 arc-second resolution Multi-Error-Removed Improved-Terrain digital
109 elevation model (MERIT DEM; Yamazaki et al., 2017).



110

111 Figure 1. The color of each 0.1° grid indicates the radial radius to find (a) one, (b) 20, and (c) 30 neighboring stations
112 for precipitation (a-c) and temperature (d-f).



113 3. Methodology

114 The estimate of a variable at a specific location and time step can be regarded as a random value following a probability
115 distribution. The probability density functions (PDFs) of variables such as the Tmean and Trange, can be approximated
116 using the normal distribution. Their value x for the target location and time step is expressed as:

$$x \sim N(\mu, \sigma^2) \quad (1)$$

117 where μ is the mean value and σ is the standard deviation. The probabilistic estimation of Tmean and Trange can be
118 realized by sampling from this distribution. In a spatial meteorological dataset, the distribution parameters vary with
119 space and time, and the variability is related to the nature of variables and gridding (interpolation) methods. The
120 performance of gridding methods is critical because accurate estimation of μ can reduce systematic bias and smaller
121 σ means narrower spread.

122 Precipitation is different from Tmean and Trange because it can be intermittent from local to synoptic scales and its
123 distribution is both highly skewed and bounded at zero. Following Papalexiou (2018) and Newman et al. (2019b), the
124 cumulative density function (CDF) of precipitation can be expressed as below:

125

$$F_X(x) = (1 - p_0)F_{X|X>0}(x) + p_0, \text{ for } x \geq 0 \quad (2)$$

126 where $F_X(x)$ is the CDF for $x \geq 0$, $F_{X|X>0}(x)$ is the CDF for $x > 0$, and p_0 is the probability of zero precipitation.
127 The probability of precipitation (PoP) is $1 - p_0$. The CDF $F_{X|X>0}(x)$ is often approximated using the normal
128 distribution after applying suitable transformation functions to observed precipitation. Clark and Slater (2006) perform
129 the normal quantile transformation using an empirical CDF from station observations. Newman et al. (2015) apply a
130 power-law transformation. Newman et al. (2019b) adopts the Box-Cox transformation, that is,

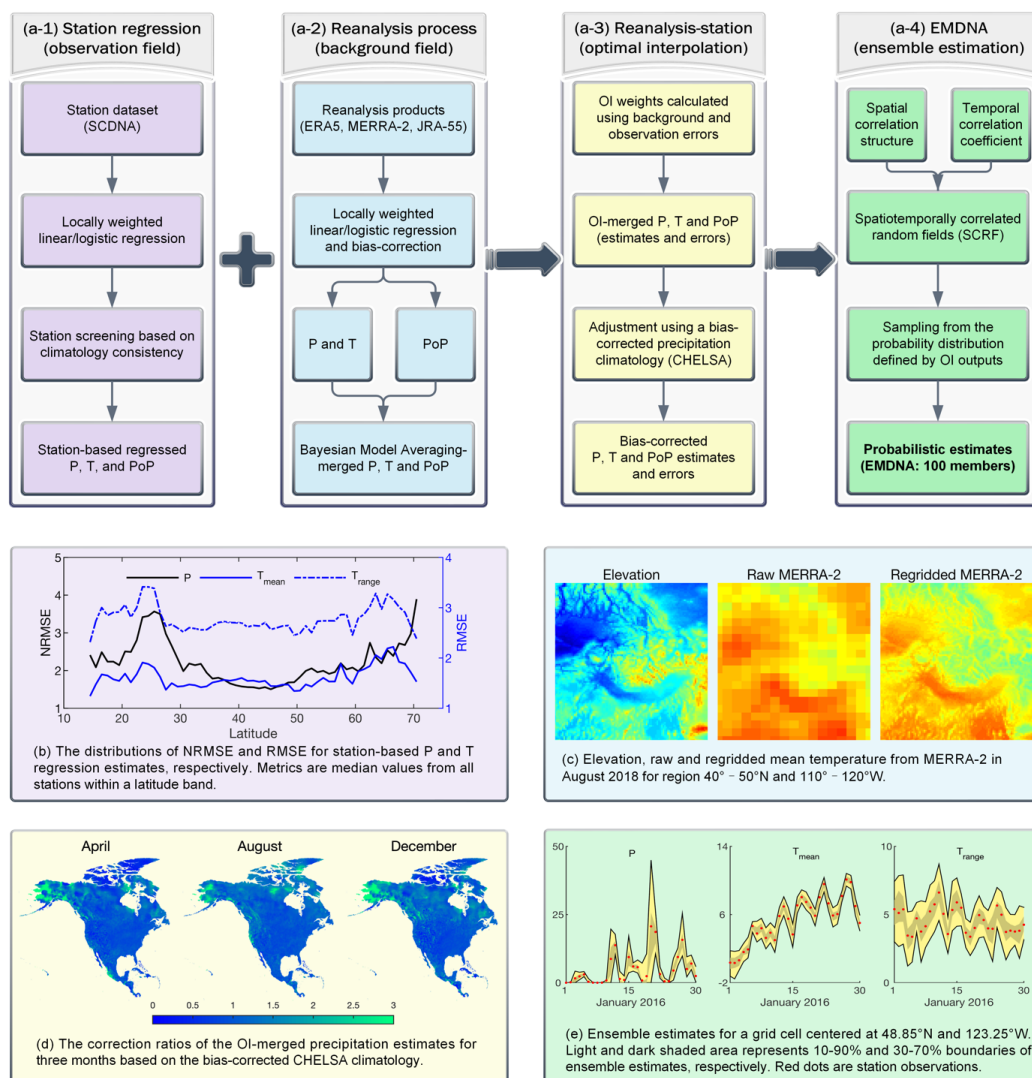
$$x' = \frac{x^\lambda - 1}{\lambda} \quad (3)$$

131 where λ is set to 1/3 following Newman et al. (2019b) and Fortin et al. (2015). Eq. (1) applies to x' , enabling the
132 probabilistic estimation of precipitation. Unlike Newman et al. (2019b) that uses transformed precipitation throughout
133 the production, this study only uses Box-Cox transformation when the assumption of normality is necessary (Sect.
134 3.2.4 and 3.3) to reduce the error introduced by the back transformation. The limitations and alternative choices of
135 precipitation transformation are discussed in Sect. 5.2.

136 In summary, seven space- and time-varying parameters (μ and σ for three variables and PoP) should be obtained to
137 realize probabilistic estimation. Our method to develop probabilistic meteorological estimates is summarized in Fig.
138 2a. We apply four main steps to produce EMDNA: (1) station-based regression estimates (Sect. 3.1), (2) the regridding,



139 downscaling, bias correction and merging of three reanalysis products (Sect. 3.2), (3) optimal interpolation-based
 140 merging of reanalysis and station-based regression outputs, and the bias correction of the resulting precipitation
 141 estimates (Sect. 3.3), and (4) the production of probabilistic estimates in the form of spatial meteorological ensembles
 142 (Sect. 3.4).



143

144 Figure 2. (a) The flowchart outlining the main steps for producing EMDNA. P represents precipitation and T represents
 145 temperature. (b-e) demonstrate output examples from (a-1 to -4), respectively. (b) Latitudinal distribution of the root
 146 mean square error (RMSE) for temperature and normalized RMSE (NRMSE) for precipitation (Sect. 3.1). (c) Example
 147 showing the mean temperature of MERRA-2 before and after regridding (Sect. 3.2). (d) The correction ratios



148 calculated using precipitation climatology from the bias-corrected CHELSA (Sect. 3.3). (e) Example of the ensemble-
149 based distributions of precipitation and temperature estimates from EMDNA (Sect. 3.4).

150 **3.1 Regression estimates from station data**

151 Clark and Slater (2006) and Newman et al. (2015, 2019b) use locally weighted linear regression and logistic regression
152 to obtain gridded precipitation and temperature estimates which are used as parameters in Eq. (1). However, for high-
153 latitude regions in North America where stations are scarce (Fig.1), such gridded estimates based only on station data
154 could contain large uncertainties (Fig. 2b) due to the long distances needed to assemble a sufficient sample of stations
155 to form the regressions. This study uses optimal interpolation (OI) to merge data from stations and reanalysis models.
156 In this section, we only obtain regression estimates and their errors at the locations of stations, which are used as inputs
157 to OI in Sect. 3.3.

158 **3.1.1 Locally weighted linear regression**

159 Daily precipitation amount, Tmean and Trange are estimated for all stations based on the locally weighted linear
160 regression. Let x_o be the station observation for variable X (precipitation, Tmean, and Trange), the regression estimate
161 \hat{x} for the target point and time step is obtained as below:

$$x_o = \hat{x} + \varepsilon = \beta_0 + \sum_{i=1}^n A_i \beta_i + \varepsilon \quad (4)$$

162 where A_i is the i th time-invariant attribute (or predictor variables), β_0 and β_i are regression coefficients estimated
163 using ordinary least squares, and ε is the residual (or error term). The attributes are latitude, longitude, and elevation
164 for Tmean and Trange. For precipitation, two more attributes (west-east and south-north slopes) are used to account
165 for windward and leeward slope precipitation differences. An isotropic Gaussian low-pass filter is used to smooth
166 DEM before calculating slopes, which can reduce the influence of noise in a high-resolution DEM on the large-scale
167 topographic effect of precipitation (Newman et al., 2015). Ideally the scale of this smoothing reflects the scale at
168 which terrain most directly influences precipitation or temperature spatial patterns; in this case the filter bandwidth is
169 180 km.

170 For a target station point, \hat{x} is obtained based on data from neighboring stations. Newman et al. (2015, 2019b) used
171 30 neighboring stations, without controlling for maximum station distance. The very low station density in high-
172 latitude regions makes this configuration infeasible, hence this study adopts a relatively flexible criterion for selecting
173 neighboring stations: (1) finding at most 30 stations within a fixed search radius (400 km), and (2) if fewer than 20
174 stations are found, extending the search radius until 20 stations are found. The least number is set to 20 to ensure that
175 linear/logistic regression is robust. To incorporate local dependence, a tricube weighting function is used to calculate
176 the weight $w_{i,j}$ between the target station i and the neighboring station j .



$$w_{i,j} = \left[1 - \left(\frac{d_{i,j}}{d_{max}}\right)^3\right]^3 \quad (5)$$

177 where $d_{i,j}$ is the distance between i and j , and d_{max} depends on the maximum distance ($d_{i,j}^{max}$) between i and all its
178 neighboring stations. If $d_{i,j}^{max}$ is smaller than 100 km, d_{max} is set to 100 km; otherwise, d_{max} is set to $d_{i,j}^{max} + 1$ km
179 (Newman et al., 2015, 2019b). Regression coefficients are estimated by weighted least squares method (described in
180 in Appendix A).

181 We found that a small number of observations stations show a climatology that is notably statistically different from
182 surrounding stations, which could cause an adverse effect on gridded estimates, particularly in sparsely gauged regions.
183 Strategies are designed to identify and exclude such stations (Appendix B).

184 3.1.2 Locally weighted logistic regression

185 PoP is estimated using the locally weighted logistic regression by fitting binary precipitation occurrence to spatial
186 attributes:

$$\text{PoP} = \frac{1}{1 + \exp(-\beta_0 + \sum_{i=1}^n A_i \beta_i)} \quad (6)$$

187 The attributes (A_i) are the same as those used by precipitation regression. Regression coefficients are estimated in
188 Appendix A.

189 The errors of precipitation, temperature, and PoP estimates for all stations are calculated as the difference between
190 regression estimates and station observations using the leave-one-out cross-validation procedure.

191 3.2 Regridding, correction, and merging of reanalysis datasets

192 The three reanalysis datasets (ERA5, MERRA-2, and JRA-55) have different spatial resolutions and contain
193 systematic biases. In this section, we discuss steps taken to (1) regrid all reanalysis datasets to the resolution of
194 EMDNA (0.1°), (2) perform a correction to remove the systematic bias in original estimates, and (3) merge the three
195 reanalysis datasets to produce a background field that improves over any individual reanalysis dataset, in support of
196 the reanalysis-station merging described in Sect. 3.3.

197 3.2.1 Regridding of reanalysis datasets

198 Precipitation, Tmean, and Trange are regridded to 0.1° using locally weighted regression (Fig. 2c). Latitude, longitude,
199 and elevation are used as predictor variables for simplicity. Precipitation or temperature lapse rates are implicitly
200 considered by involving elevation in the regression. Raw reanalysis data from a 5×5 space window (i.e., 25 coarse-
201 resolution grids) centered by the 0.1° target grid are used to perform the regression. Each grid is represented using its
202 center point. This regridding method has been proven effective in previous studies (Xu et al., 2015; Duan and Li, 2016;
203 Lu et al., 2020). Reanalysis estimates are also regressed to the locations of all stations to facilitate evaluation and



204 weight estimation in the following steps, which can avoid the scale mismatch caused by using point-scale observations
205 to evaluate 0.1° gridded estimates (Tang et al., 2018a).

206 We also tested other regridding methods such as the nearest neighbor, bilinear interpolation, and temperature lapse
207 rate-based downscaling (Tang et al., 2018b). Results (not shown) indicated that their performance is generally inferior
208 to the locally weighted regression with respect to several accuracy metrics.

209 3.2.2 Probability of precipitation estimation

210 Reanalysis precipitation can exhibit large biases in the number of wet days because the models often generate many
211 light precipitation events. To overcome this limitation, we designed two methods for determining the occurrence of
212 reanalysis precipitation. The first is to use positive thresholds to determine precipitation occurrence. The threshold
213 was estimated in two ways, namely by forcing reanalysis precipitation (1) to have the same number of wet days with
214 station data, or (2) to achieve the highest critical success index (CSI). Gridded thresholds can be obtained through
215 interpolation and used to discriminate between precipitation events or non-events. However, this method can only
216 obtain binary occurrence instead of continuous PoP between zero and one. The second method is based on univariate
217 logistic regression. The amount of reanalysis precipitation is used as the predictor and the binary occurrence from
218 station data is used as the predictand. The logistic regression is implemented for each reanalysis product in the same
219 way as Sect. 3.1.2. The comparison between the threshold-based method and the logistic regression-based method
220 shows the latter achieves higher accuracy. Therefore, we adopt the univariate logistic regression to estimate PoP for
221 each reanalysis product in this study. The possible bias caused by station measurements is not considered.

222 3.2.3 Bias correction of reanalysis datasets

223 Considering reanalysis products usually contain systematic bias (Mooney et al., 2011; Beck et al., 2017; Tang et al.,
224 2018b, 2020b), the linear scaling method (also known as multiplicative/additive correction factor; Teutschbein and
225 Seibert, 2012) is used to correct reanalysis precipitation, Tmean, and Trange estimates. Reanalysis PoP is not corrected
226 because station information has been incorporated in the logistic regression. Let x_r be the reanalysis estimate for
227 variable X , the corrected estimate for a target grid/point i is calculated as:

$$x_{r,i}^* = \begin{cases} x_{r,i} + \frac{\sum_{j=1}^m w_{i,j} (\bar{x}_{o,j} - \bar{x}_{r,j})}{\sum_{j=1}^m w_{i,j}} & \text{additive correction} \\ x_{r,i} \frac{\sum_{j=1}^m w_{i,j} \bar{x}_{o,j}}{\sum_{j=1}^m w_{i,j} \bar{x}_{r,j}} & \text{multiplicative correction} \end{cases} \quad (7)$$

228 where $x_{r,i}^*$ is the corrected reanalysis estimate, $w_{i,j}$ is the distance-based weight (Eq. (5)), and $\bar{x}_{o,j}$ and $\bar{x}_{r,j}$ are the
229 climatological mean for each month (e.g., all January from 1979 to 2018) from station observations and reanalysis
230 estimates for the j th neighboring station, respectively. The additive correction is used for Tmean and Trange, and the
231 multiplicative correction is used for precipitation. The number of neighboring stations (m) is set to 10, which is smaller



232 than that used for linear or logistic regression (Sect. 3.1) but should be enough for bias correction. The upper bound
233 of $\frac{\bar{x}_{o,j}}{\bar{x}_{r,j}}$ is set to 10 to avoid over-correction in some cases (Hempel et al., 2013).

234 Linear scaling can also be performed at monthly (Arias-Hidalgo et al., 2013; Hernegger et al., 2018; Willkofer et al.,
235 2018) or daily (Vila et al., 2009; Habib et al., 2014) scales by replacing $\bar{x}_{o,j}$ and $\bar{x}_{r,j}$ by monthly mean (e.g., January
236 in one year) or daily values. We compared the performance of corrections at different scales and found that monthly-
237 or daily-scale corrections acquire more accurate estimates than the climatological correction. The climatological
238 correction was adopted because (1) it preserves the absolute/relative trends better than daily or monthly corrections,
239 and (2) the OI merging (Sect. 3.3) adjusts daily variability of estimates, which compensates for the limitation of
240 climatological correction and makes daily/monthly-scale correction unnecessary.

241 Quantile mapping is another widely used correction method (Wood et al., 2004; Cannon et al., 2015). We compared
242 quantile mapping and linear scaling and found that they are similar in statistical accuracy, while quantile mapping
243 achieves better probability distributions with much smaller Hellinger distance (Hellinger, 1909) which is a metric used
244 to quantify the similarity between estimated and observed probability distributions. Nevertheless, quantile mapping
245 could result in spatial smoothing of precipitation and temperature, particularly in high-latitude regions where stations
246 are few. For example, Ellesmere Island, the northernmost island of the Canadian Arctic Archipelago, usually shows
247 lower temperature in inland regions due to orographic uplift. However, quantile mapping will erase this gradient
248 because reanalysis grids for this island are corrected based on almost the same reference stations. To ensure the
249 authenticity of spatial distributions, quantile mapping is not used in this study.

250 3.2.4 Merging of reanalysis datasets

251 The three reanalysis products are merged using the Bayesian Model Averaging (BMA, Hoeting et al., 1999), which
252 has proved to be effective in fusing multi-source datasets (Chen et al., 2015; Ma et al., 2018a, 2018b). According to
253 the law of total probability, the PDF of the BMA estimate can be written as:

$$p(E) = \sum_{r=1}^3 p(E|x_r^*, x_o) \cdot p(x_r^*|x_o) \quad (8)$$

254 where E is the ensemble estimate, x_r^* ($r=1, 2, 3$) is the bias-corrected estimate from three reanalysis products,
255 $p(E|x_r^*, x_o)$ is the predicted PDF based only on a specific reanalysis product, and $p(x_r^*|x_o)$ is the posterior probability
256 of reanalysis products given the station observation x_o . The posterior probability $p(x_r^*|x_o)$ can be identified as the
257 fractional BMA weight w_r with $\sum_{r=1}^3 w_r = 1$. BMA prediction can be written as the weighted sum of individual
258 reanalysis products.

259 For Tmean and Trange, $p(E|x_r^*, x_o)$ can be regarded as the normal distribution $g(E|\theta_r)$ defined by the parameter
260 $\theta_r = \{\mu_r, \sigma_r^2\}$, where μ_r is the mean and σ_r^2 is the variance (Duan and Phillips, 2010). For precipitation, if we apply



261 Box-Cox transformation (Eq. (3)) to positive events (>0) and exclude zero events, its distribution is approximately
 262 normal, and $p(E|x_r^*, x_o)$ can be represented using $g(E|\theta_r)$. Therefore, Eq. (8) can be written as:

$$p(E) = \sum_{r=1}^3 w_r \cdot g(E|\theta_r) \quad (9)$$

263 There are different approaches to infer w_r and θ_r (Schepen and Wang, 2015). This study uses the log-likelihood
 264 function to estimate the parameters (Duan and Phillips, 2010; Chen et al., 2015; Ma et al., 2018b). The Expectation-
 265 Maximization algorithm (Raftery et al., 2005) can be applied to estimate parameters by maximizing the likelihood
 266 function. BMA weights are obtained for all stations and each month. Gridded weights are obtained using the inverse
 267 distance weighting interpolation.

268 Merging multiple datasets could affect the probability distributions and extreme characteristics of original datasets.
 269 This is not a major concern because the merged reanalysis data are further adjusted by station data in OI merging (Sect.
 270 3.3), a later step in the EMDNA process. Also, the probabilistic estimation of ensemble members (Sect. 3.4) has a
 271 large effect on estimates of extreme events.

272 Gridded errors of BMA-merged estimates are necessary to enable optimal interpolation (Sect. 3.3). The error
 273 estimation is realized using a two-layer cross-validation (Appendix C).

274 3.3 Optimal Interpolation-based merging of reanalysis and station data

275 3.3.1 Optimal Interpolation

276 OI has proven to be effective in merging multiple datasets (Sinclair and Pegram, 2005; Xie and Xiong, 2011) and has
 277 been applied in operational products such as CaPA (Mahfouf et al., 2007; Fortin et al., 2015) and the China Merged
 278 Precipitation Analysis (CMPA, Shen et al., 2014, 2018). Let x_A be the OI analysis estimate. The OI analysis estimate
 279 ($x_{A,i}$) for a target grid/point i and time step is obtained by adding an increment to the first guess of the background
 280 ($x_{B,i}$). The increment is a weighted sum of the difference between observation and background values at neighboring
 281 stations.

$$x_{A,i} = x_{B,i} + \sum_{j=1}^m w_j (x_{O,j} - x_{B,j}) \quad (10)$$

282 where $x_{O,j}$, $x_{B,j}$, and w_j are the observed value (subscript O), background value (subscript B), and weight for the j th
 283 neighboring station. Let x_T be the true value, the errors of observed and background values are $\varepsilon_{O,j} = x_{O,j} - x_{T,j}$ and
 284 $\varepsilon_{B,j} = x_{B,j} - x_{T,j}$ (or $\varepsilon_{B,i} = x_{B,i} - x_{T,i}$), respectively. Assuming that (1) the observation and background errors are
 285 unbiased with an expectation of zero and (2) there is no correlation between background and observation errors, the
 286 weights that minimize the variance of the analysis errors can be obtained by solving:



$$\mathbf{w}(\mathbf{R} + \mathbf{B}) = \mathbf{b} \quad (11)$$

287 where \mathbf{w} is the vector of w_j ($j = 1, 2, \dots, m$), \mathbf{R} and \mathbf{B} are $m \times m$ covariance matrices of $\varepsilon_{O,j}$ and $\varepsilon_{B,j}$, respectively,
288 and \mathbf{b} is the $m \times 1$ vector of covariance between $\varepsilon_{B,i}$ and $\varepsilon_{B,j}$. The background provided by reanalysis models
289 assimilates observations in the production and is corrected in a way using station data (described in Sect. 3.2.3), which
290 may affect the soundness of the second assumption. The effect of this slight violation, however, is rather small
291 according to our results and previous studies (Xie and Xiong, 2011; Shen et al., 2014b, 2018).

292 Different approaches can be used to implement OI. For example, Fortin et al. (2015) use raw station observations as
293 x_o , and assumes that the background error is a function of error variance and correlation length, and the observation
294 error is a function of error variance. The variances and correlation length are obtained by fitting a theoretical variogram
295 using station observations. Xie and Xiong (2011) and Shen et al. (2014) use station-based gridded estimates as x_o ,
296 and assume that the background error variance is a function of precipitation intensity, the cross-correlation of
297 background errors is a function of distance, and the observation error variance is a function of precipitation intensity
298 and gauge density. The parameters of those functions are estimated based on station data in densely gauged regions.

299 In this study, we adopt a novel design that calculates weights based on error estimation, a feature that is enabled by
300 the probabilistic nature of the observational dataset. Regression estimates and their errors at station points (Sect. 3.1)
301 are used as x_o and ε_o , respectively. BMA-merged reanalysis estimates and their errors (Sect. 3.2) are used as x_B and
302 ε_B , respectively. We do not use gridded regression estimates because (1) $x_{O,j} - x_{B,j}$ will show weak variation if
303 neighboring stations are replaced by neighboring grids, and (2) estimates of weights \mathbf{w} could be unrealistic because
304 of the spatial smoothing of interpolated regression errors. The advantages of this design are (1) weights and inputs
305 closely match each other and (2) weights in sparsely gauged regions are not determined by parameters fitted in densely
306 gauged regions.

307 The Box-Cox transformation is applied to precipitation estimates. Then, precipitation, PoP, Tmean, and Trange
308 estimates provided by OI are used as μ and PoP required for generating meteorological ensembles.

309 3.3.2 Error of OI-merged estimates

310 Variance is a necessary parameter to enable ensemble estimation. The variance σ^2 is represented using the mean
311 squared error of OI estimates in this study. First, the error of OI analysis estimates ($\varepsilon_A = x_A - x_o$) is obtained for all
312 stations using the leave-one-out strategy. Then, the σ_i^2 for the i th grid is obtained as a weighted sum of squared errors
313 from neighboring stations:

$$\sigma_i^2 = \frac{\sum_{j=1}^m w_{i,j} (\varepsilon_{A,j})^2}{\sum_{j=1}^m w_{i,j}} \quad (12)$$

314 where $\varepsilon_{A,j}$ is the difference between the station observation and OI estimate at the j th neighboring station, and $w_{i,j}$ is
315 the weight (Eq. (5)).



316 3.3.3 Correction of precipitation under-catch

317 Considering station precipitation data usually contain measurement errors such as wind-induced under-catch
318 particularly in high-latitude and mountainous regions, OI-merged precipitation is further adjusted using the bias-
319 corrected precipitation climatology produced by Beck et al. (2020). This climatology infers the long-term precipitation
320 using a Budyko curve and streamflow observations. Three corrected datasets are provided, including WorldClim,
321 version 2 (WorldClim V2; Fick and Hijmans, 2017), the Climate Hazards Group Precipitation Climatology, version 1
322 (CHPclim V1; Funk et al., 2015) and Climatologies at High Resolution for the Earth's Land Surface Areas, version
323 1.2 (CHELSA V1.2; Karger et al., 2017). The water balance-based method of Beck et al. (2020) considers all
324 measurement errors (e.g., under-catch and wetting/evaporation loss) as a whole and under-catch is the major error
325 source in many regions.

326 Although the three datasets show similar precipitation distributions after bias correction, CHELSA V1.2 is used
327 because its period (1979–2013) is most similar to our study period (1979–2018). The correction of OI-merged
328 precipitation is performed in two steps: (1) the ratio between bias-corrected CHELSA V1.2 and OI-merged long-term
329 monthly precipitation is calculated at the 0.1° resolution during 1979–2013, and (2) daily OI-merged precipitation
330 estimates during 1979–2018 are scaled using the corresponding monthly ratio map. The bias correction notably
331 increases precipitation in northern Canada and Alaska (Fig. 2d) where under-catch of precipitation is often large.

332 3.4 Ensemble generation

333 3.4.1 Spatiotemporally correlated random fields

334 Spatially correlated random fields (SCRFs) are used to sample from the probability distributions of precipitation and
335 temperature. The SCRFs are produced using the following three steps. First, the spatial correlation structure is
336 generated based on an exponential correlation function:

$$c_{i,j} = \exp\left(-\frac{d_{i,j}}{C_{len}}\right) \quad (13)$$

337 where $d_{i,j}$ is the distance between grids i and j , and C_{len} is the spatial correlation length determined for each
338 climatological month based on regression using station data for precipitation, Tmean, and Trange, separately. The
339 spatial correlation structure is generated using the conditional distribution approach. Every point is conditioned on
340 previously generated points which are determined using a nested simulation strategy to improve the calculation
341 efficiency (Clark and Slater, 2006).

342 Second, the spatially correlated random field (\mathbf{R}_t) for the t th time step is generated by sampling from the normal
343 distribution with the mean value and standard deviation depending on the random numbers of previously generated
344 grids (Clark and Slater, 2006).



345 Third, the SCRF is generated by incorporating spatial and temporal correlation relationships. Let ρ_{TM} and ρ_{TR} be the
 346 lag-1 auto-correlation for Tmean and Trange, respectively, ρ_{CR} be the cross-correlation between Trange and
 347 precipitation, $\mathbf{R}_{t-1, TM}$, $\mathbf{R}_{t-1, TR}$ and $\mathbf{R}_{t-1, PR}$ be the SCRF for the $(t-1)$ th time step for Tmean, Trange, and precipitation,
 348 respectively, the SCRF for t th time step following (Newman et al., 2015) is written as:

$$\begin{cases} \mathbf{R}_{t, TM} = \rho_{TM} \mathbf{R}_{t-1, TM} + \sqrt{1 - \rho_{TM}^2} \mathbf{R}_{t-1, TM} \\ \mathbf{R}_{t, TR} = \rho_{TR} \mathbf{R}_{t-1, TR} + \sqrt{1 - \rho_{TR}^2} \mathbf{R}_{t-1, TR} \\ \mathbf{R}_{t, PR} = \rho_{CR} \mathbf{R}_{t-1, TR} + \sqrt{1 - \rho_{CR}^2} \mathbf{R}_{t-1, PR} \end{cases} \quad (14)$$

349 3.4.2 Probabilistic estimation

350 Probabilistic estimates are produced using the probability distribution $N(\mu, \sigma^2)$ in Eq. (1) and \mathbf{R} in Eq. (14). For
 351 Tmean and Trange, the SCRF (\mathbf{R}_{TM} and \mathbf{R}_{TR}) is directly used as the standard normal deviate (R_X). The estimate (x_e)
 352 for the ensemble member e is written as:

$$x_e = \mu + R_X \cdot \sigma \quad (15)$$

353 For precipitation, an additional step is to judge whether an event occurs or not according to OI-merged PoP and the
 354 estimated probability from the SCRF. Let $F_N(x)$ be the CDF of the standard normal distribution, $F_N(R_{PR})$ is the
 355 cumulative probability corresponding to the random number R_{PR} . If $F_N(R_{PR})$ is larger than p_0 , the scaled cumulative
 356 probability of precipitation (p_{cs}) is calculated as:

$$p_{cs} = \frac{F_N(R_{PR}) - p_0}{1 - p_0} \quad (16)$$

357 The probabilistic estimate for precipitation can be expressed as:

$$x_e = \begin{cases} 0 & \text{if } F_N(R_{PR}) \leq p_0 \\ \mu + F_N^{-1}(p_{cs}) \cdot \sigma & \text{if } F_N(R_{PR}) > p_0 \end{cases} \quad (17)$$

358 3.5 Evaluation of probabilistic estimates

359 Independent stations that are not used in SCDNA are used to evaluate EMDNA because the leave-one-out strategy is
 360 too time-consuming for evaluating probabilistic estimates. GHCN-D stations with precipitation or temperature records
 361 less than eight years are extracted because SCDNA restricts attention to stations with at least eight-year records. In
 362 total, 15,018 precipitation stations and 2,455 temperature stations are available for independent testing.



363 The Brier skill score (BSS; Brier, 1950) is used to evaluate probabilistic precipitation estimates. The continuous ranked
364 probability skill score (CRPSS) is used to evaluate probabilistic temperature estimates. Their definitions are described
365 in Appendix D.

366 Furthermore, the reliability and discrimination diagrams are used to assess the behavior of probabilistic precipitation
367 estimates. The reliability diagram shows the conditional probability of an observed event (precipitation above a
368 threshold) given the probability of probabilistic precipitation estimates. In a reliability diagram, a perfect match has
369 all points located on the 1-1 line. The discrimination diagram shows the PDF of probabilistic precipitation estimates
370 for different observed categories. For precipitation, two categories are defined: events or non-events, i.e., observed
371 precipitation above or below a threshold. The difference between PDF curves of events or non-events represents the
372 degree of discrimination. Larger discrimination is preferred. The PDF for non-event/event should be maximized at the
373 probability of zero/one.

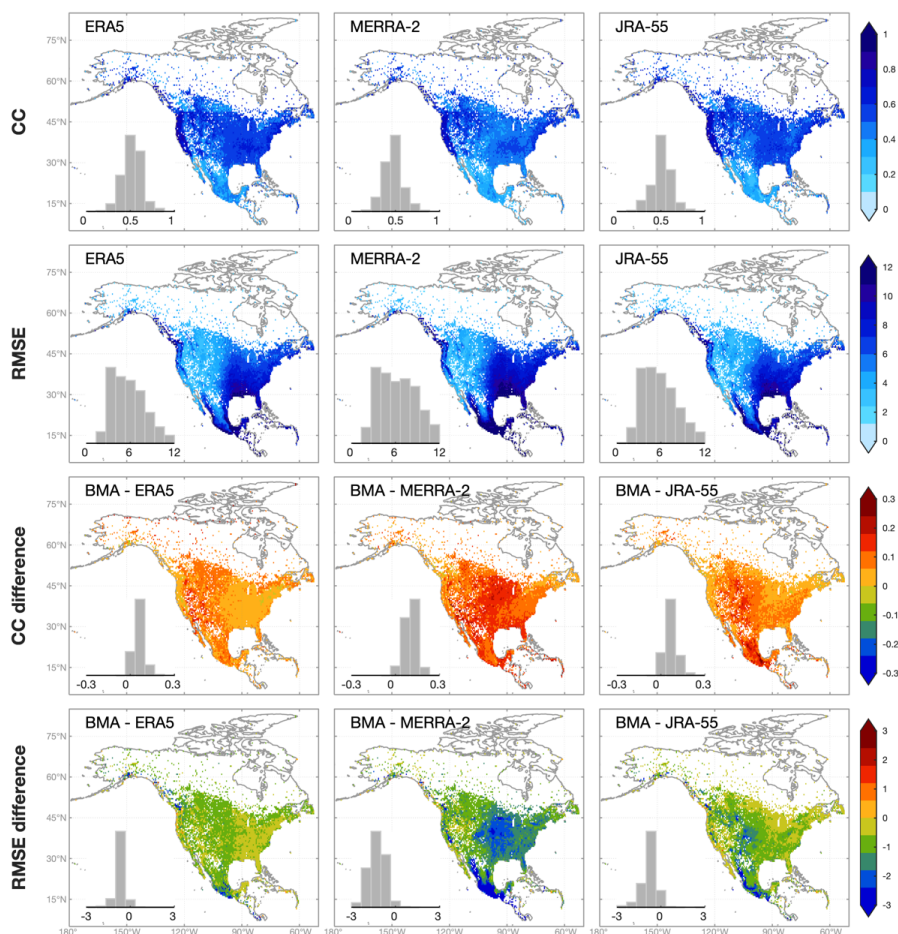
374 **4. Results**

375 **4.1 Comparison between raw and merged reanalysis estimates**

376 The three raw reanalysis estimates are regridded, corrected for bias, and merged. In this section, we directly compare
377 raw and BMA-merged estimates. The evaluation is performed for all stations using the two-layer cross-validation
378 strategy. The correlation coefficient (CC) and root mean square error (RMSE) are used as evaluation metrics.

379 For precipitation, the three reanalysis products show the highest CC in CONUS and the lowest CC in Mexico (Fig. 3).
380 The slight spatial discontinuity of CC along the Canada-USA border and the USA-Mexico border (Fig. 3 and 6) is
381 caused by the inconsistent reporting time of stations. Daily precipitation from reanalysis products is accumulated from
382 0 to 24 UTC, while stations from different countries or regions usually have different UTC accumulation periods
383 (Beck et al., 2019; Tang et al., 2020a). The distributions of RMSE agrees with those of precipitation amounts with
384 higher values in the southern corner and west coast of North America and western CONUS. Overall, ERA5
385 outperforms MERRA-2 followed by JRA-55.

386 BMA-merged precipitation estimates show higher accuracy than all reanalysis products (Fig. 3). For ERA5 and JRA-
387 55, the improvement of CC and RMSE is the most evident in the Rocky Mountains, while for MERRA-2, the largest
388 improvement occurs in central CONUS. ERA5 is the closest to BMA estimates concerning CC and RMSE. The
389 improvement of BMA estimates against ERA5 is more prominent in the high-latitude regions. Specifically, the mean
390 CC increases by 0.05 and 0.07 in regions southern and northern to 55°N, respectively. The corresponding decrease of
391 mean RMSE is 0.72 and 0.89 mm/d, respectively.



392

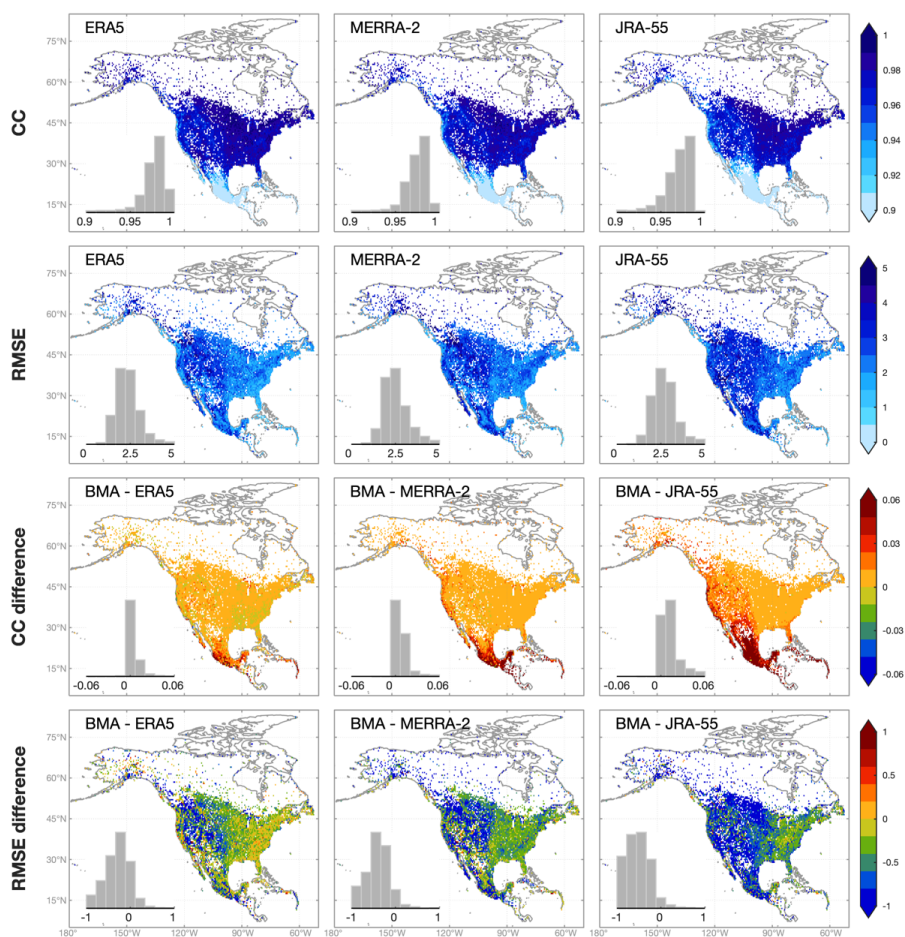
393 Figure 3. The spatial distributions and histograms of CC (the first row) and RMSE (the second row) based on raw
394 reanalysis precipitation estimates (ERA5, MERRA-2, and JRA-55). The improvement of BMA-merged estimates
395 against raw reanalysis estimates is shown in the third and fourth rows. The grid resolution is 0.5°. For each 0.5° grid
396 point, the median value of all stations located within the grid is shown.

397 The CC of reanalysis Tmean estimates is close to one in most regions of North America (Fig. 4) and still above 0.9 in
398 Mexico where the CC is the lowest. According to RMSE, Tmean estimates have the largest error in western North
399 America because coarse-resolution raw reanalysis estimates cannot reproduce the variability of temperature caused
400 by elevation variations. The rank of three reanalysis products for Tmean is the same as that for precipitation with
401 ERA5 being the best one. BMA estimates show higher CC than reanalysis products particularly in Mexico, while the
402 improvement of RMSE is the most notable in the Rocky Mountains. For a few stations, the RMSE of BMA estimates

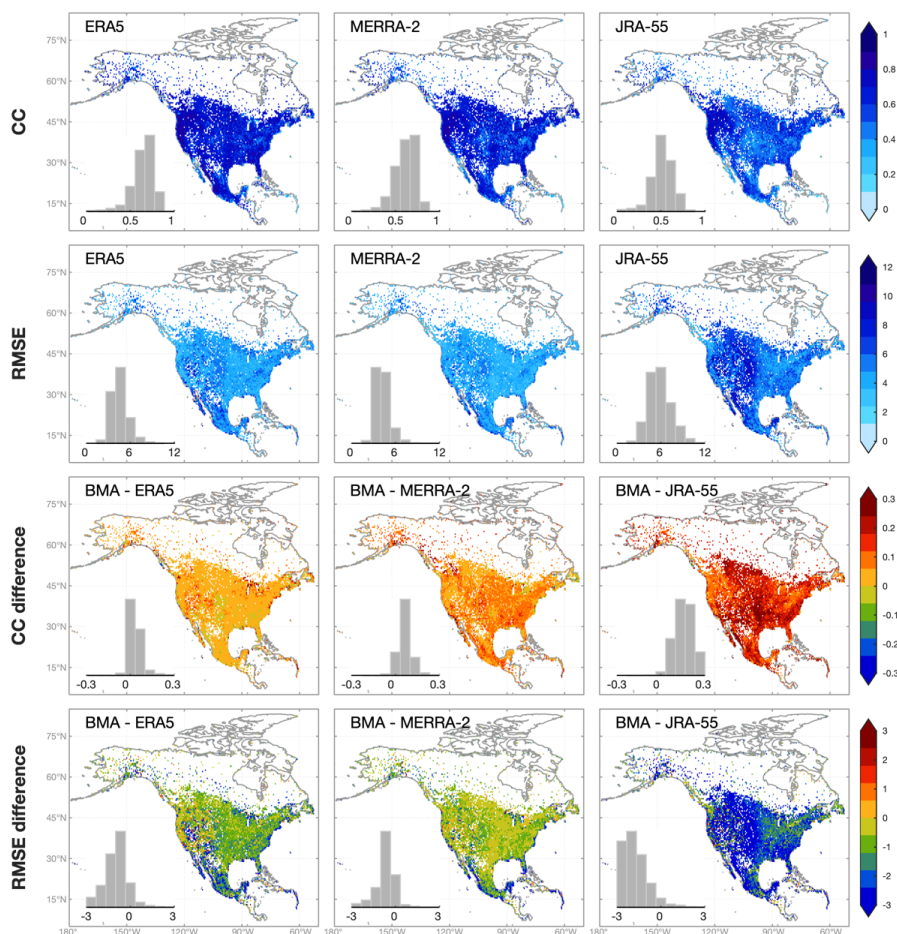


403 is slightly worse than raw reanalysis estimates (Fig. 4) because the downscaling of reanalysis temperature could
404 occasionally magnify the error in low-altitude regions (Tang et al., 2018b).

405 For Trange, BMA estimates show much larger improvement than Tmean, while the differences of CC and RMSE are
406 relatively evenly distributed (Fig. 5). The improvement of BMA estimates against JRA-55 estimates is especially large.
407 In general, BMA is effective in improving the accuracy of reanalysis precipitation and temperature estimates.



408
409 Figure 4. Same with Figure 3, but for mean temperature.



410

411 Figure 5. Same with Figure 3, but for daily temperature range.

412 4.2 The performance of optimal interpolation

413 Optimal interpolation is used to combine station-based estimates with reanalysis estimates. The performance of OI-
414 merged precipitation and temperature estimates is compared to the background (BMA-merged reanalysis estimates;
415 Fig. 6) and observation (station-based regression estimates; Fig. 7) inputs. To better show the spatial variations of the
416 improvement of OI estimates, RMSE for precipitation and Trange is normalized using the mean value (termed as
417 NRMSE), while Tmean is evaluated using RMSE.

418 Overall, OI estimates are more accurate than merged reanalysis or station regression estimates for all variables across
419 North America. Comparing OI estimates to reanalysis estimates, for precipitation, Tmean, and Trange, the mean CC
420 is improved by 0.24, 0.02, and 0.15, respectively, and the mean RMSE is reduced by 1.88 mm/d, 0.52°C, and 0.87°C,

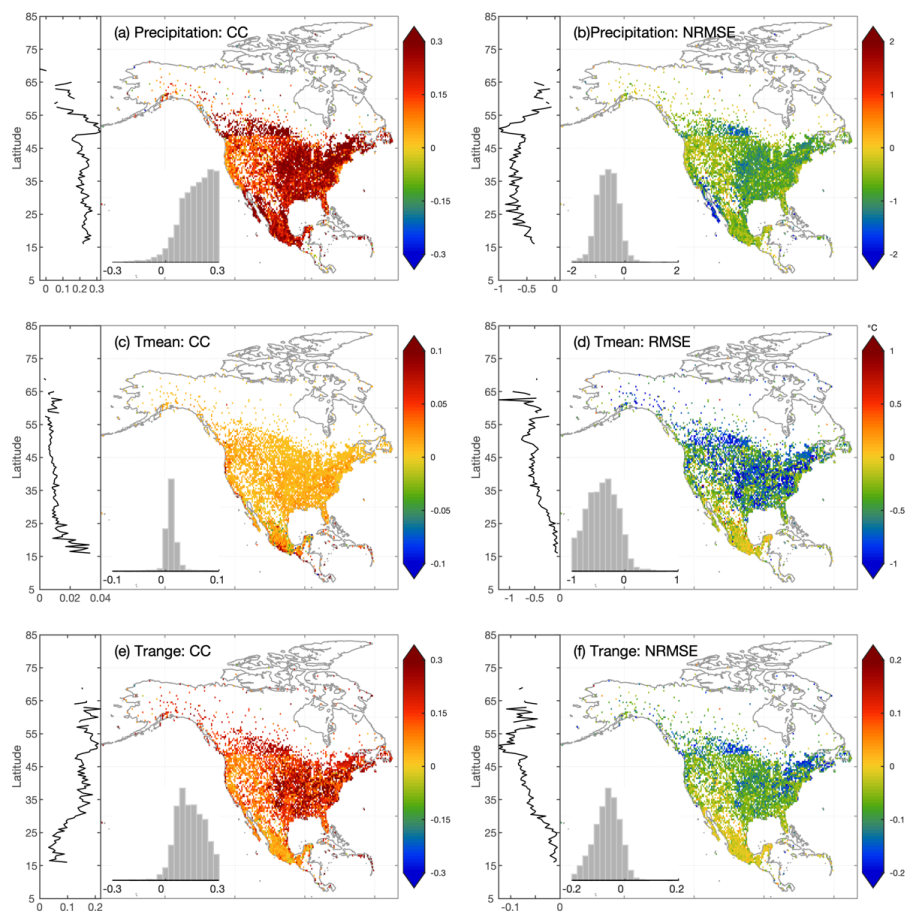


421 respectively. The improvement of OI estimates against station estimates is smaller with the mean CC increasing by
422 0.06, 0.01 and 0.05, and the mean RMSE decreasing by 0.56 mm/d, 0.18°C, and 0.29°C for precipitation, Tmean, and
423 Trange, respectively.

424 OI can utilize the complementarity between station and reanalysis estimates. For example, according to CC, the
425 improvement of OI estimates against reanalysis estimates is larger in the eastern than the western CONUS, while the
426 improvement against station estimates is larger in western than eastern CONUS. This means that although station
427 estimates generally show higher accuracy reanalysis estimates, station estimates face more severe quality degradation
428 in mountainous regions. Moreover, the latitudinal curves of CC and NRMSE in Fig. 6 and 7 indicate that the
429 improvement of OI estimates against reanalysis estimates decreases as the latitude increases from southern CONUS
430 to northern Canada, while the improvement against station estimates shows a reverse trend.

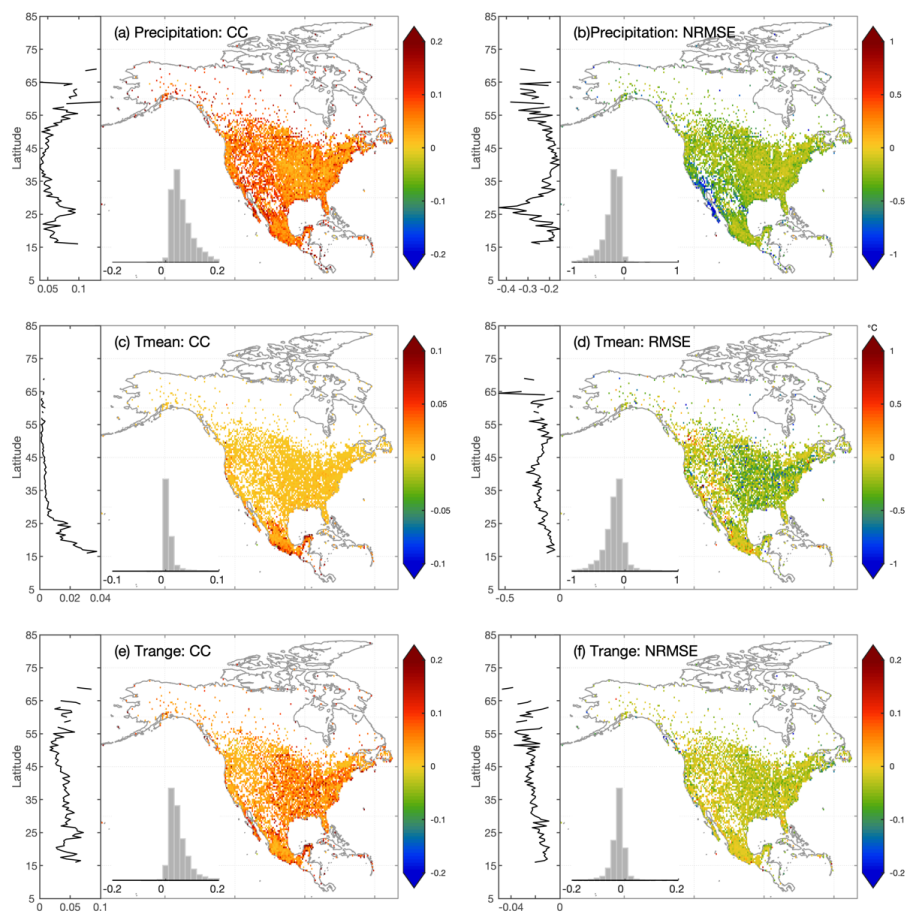
431 For Tmean, the CC improvement for OI estimates is the largest in Mexico and decreases from low to high latitudes,
432 while based on RMSE, the improvement increases with latitude. For Trange, the latitudinal variation exhibits a similar
433 pattern with precipitation for regions north of 50°N, with larger/smaller improvement in higher latitudes against
434 station/reanalysis estimates. For regions south of 50°N, the improvement of CC and NRMSE against station estimates
435 shows different trends.

436 The latitudinal variations in Fig. 6 and 7 are related to station densities (Fig. 8). Station-based estimates often have
437 lower accuracy in regions with scarce stations (i.e., high-latitude North America), while reanalysis estimates could
438 have less dependence on station densities due to the compensation of physically-based models. For precipitation, the
439 improvement of OI estimates against regression estimates increases with the distance according to both CC and
440 NRMSE, while the improvement against reanalysis estimates shows an inverse trend (Fig. 8). The shaded area figure
441 within Fig. 8 shows that most stations can find the 20 neighboring stations within the search radius of 20-100 km.
442 However, as the distance increases beyond 200 km, the number of stations becomes very small while the number of
443 grids is still large. For Tmean, the trend with distance is not obvious probably because it is usually easier to interpolate
444 Tmean observations due to its strong linkage with elevation and latitude. For Trange, the improvement against
445 reanalysis and station estimates both increases with the distance. The results show that OI merging is particularly
446 useful in sparsely gauged regions.



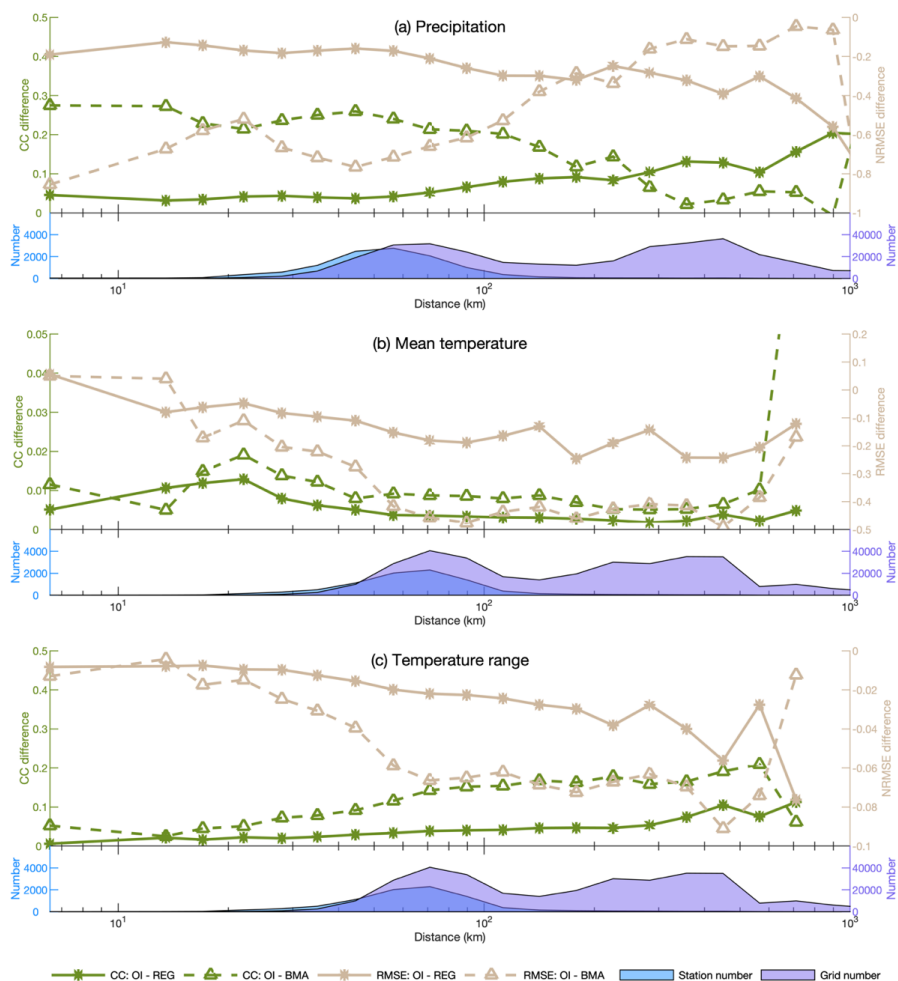
447

448 Figure 6. The differences of (a) CC and (b) NRMSE (normalized RMSE) between OI-merged precipitation estimates
449 and BMA-merged reanalysis precipitation estimates. The latitudinal distributions of metrics are attached on the left
450 side, showing the median value for 0.5° latitude bands. (c-d) are the same with (a-b) but for mean temperature and
451 RMSE is not normalized. (e-f) are the same with (a-b) but for daily temperature range.



452

453 Figure 7. Similar with Figure 6, but the differences are between OI-merged precipitation estimates and station-based
454 regression precipitation estimates.



455

456 Figure 8. The improvement of OI-based station-reanalysis merged estimates against station-based regression (REG)
 457 and BMA-merged reanalysis (BMA). The logarithmic X-axis shows the distance between the target station/grid and
 458 its 20th distant neighboring station. A larger distance represents a lower station density. The shaded area chart shows
 459 the numbers of stations and grid points corresponding to the same distance, which is the same for mean temperature
 460 and temperature range.

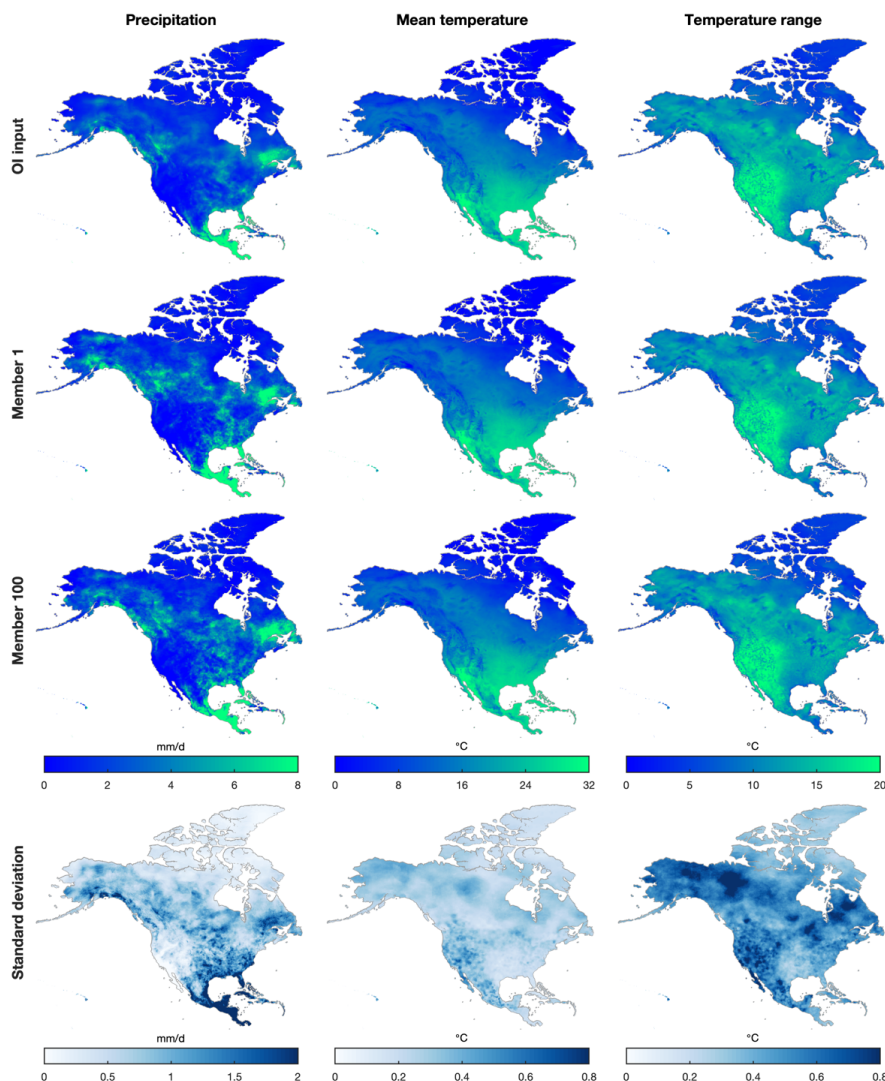
461 4.3 Evaluation of probabilistic estimates

462 The distributions of the OI and ensemble precipitation, Tmean, and Trange estimates in June 2016 are shown in Fig.
 463 9. Compared with OI precipitation estimates, ensemble precipitation estimates show generally consistent but less
 464 smooth distributions because of the relatively short spatial correlation length in the warm season. For Tmean and



465 Trange, OI and ensemble estimates show very similar spatial distributions. Precipitation shows the largest standard
466 deviation, while Tmean shows the smallest, because the standard deviation is determined by the errors of OI estimates.

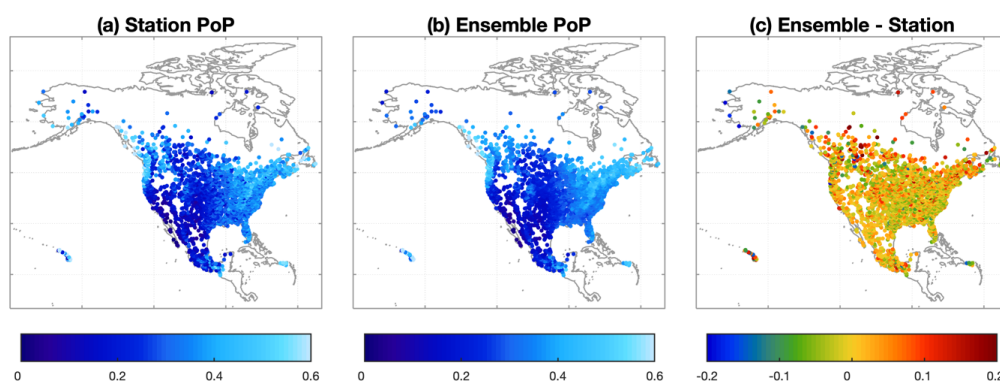
467 The PoP from station observations and ensemble estimates is compared based on stations with at least 5-year-long
468 records from 1979 to 2018 (Fig. 10). The comparison cannot represent climatological PoP (Newman et al., 2019b)
469 due to short time length of independent stations (Sect. 3.5). Overall, EMDNA estimates show similar PoP distributions
470 with station observations. The PoP in Canada is slightly overestimated because (1) the quality of EMDNA is lower in
471 regions with fewer stations and (2) point-scale station observations could underestimate the PoP at a larger scale (e.g.,
472 0.1° grids) as shown by Tang et al. (2018a).



473



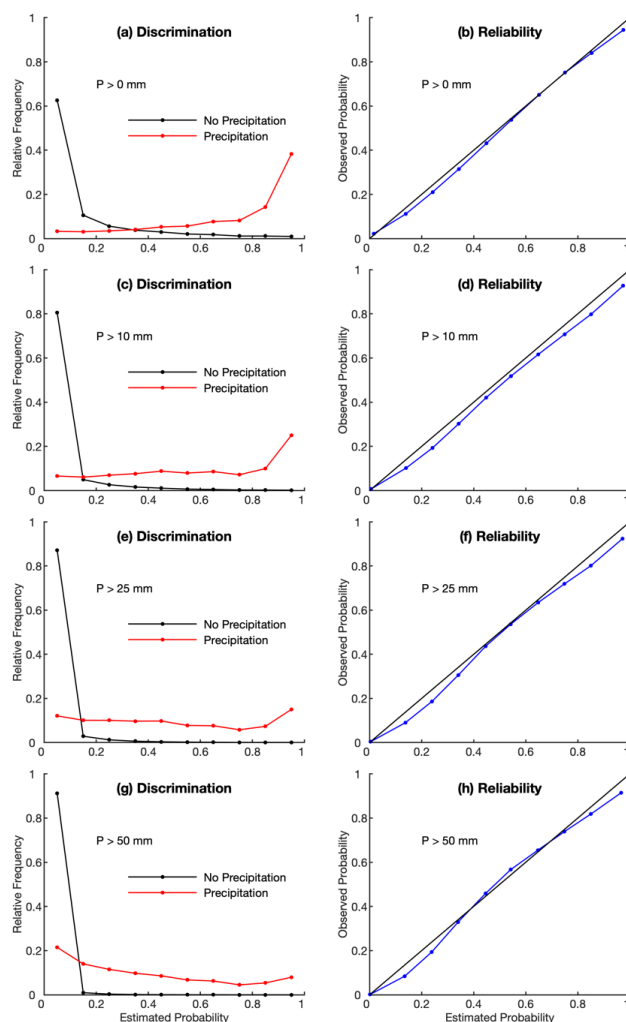
474 Figure 9. The distributions of average values from precipitation (the first column), mean daily temperature (the second
475 column), and daily temperature range (the third column) averaged over the period 1-30 June 2016. The first to third
476 rows represent estimates from OI-merged inputs, ensemble member 1, and ensemble member 100. The fourth row
477 represents the standard deviation of all the 100 members for one month (June 2016).



478

479 Figure 10. The probability of precipitation (PoP) from (a) station observations and (b) concurrent EMDNA ensemble
480 estimates with their differences shown in (c). Stations with at least 5-year-long records from 1979 to 2018 are involved
481 in the comparison.

482 The discrimination diagram (Fig. 11) shows that ensemble precipitation assigns the highest occurrence frequency at
483 the lowest estimated probability for non-precipitation events, and the performance becomes better as the threshold
484 increases from 0 to 50 mm. For precipitation events, ensemble estimates show the highest frequency at the highest
485 estimated probability for the thresholds of 0, 10, and 25 mm, while as the threshold increases, the frequency curve
486 becomes skewed to the lower estimated probability. This problem is also seen in Clark and Slater (2006) and Newman
487 et al. (2015). Ensemble precipitation shows good reliability for all precipitation thresholds with the points located at
488 or close to the 1-1 line (Fig. 11). At low and high estimated probabilities of occurrence, ensemble precipitation shows
489 slight wet bias. The reliability performance does not show clear dependence with thresholds.



490

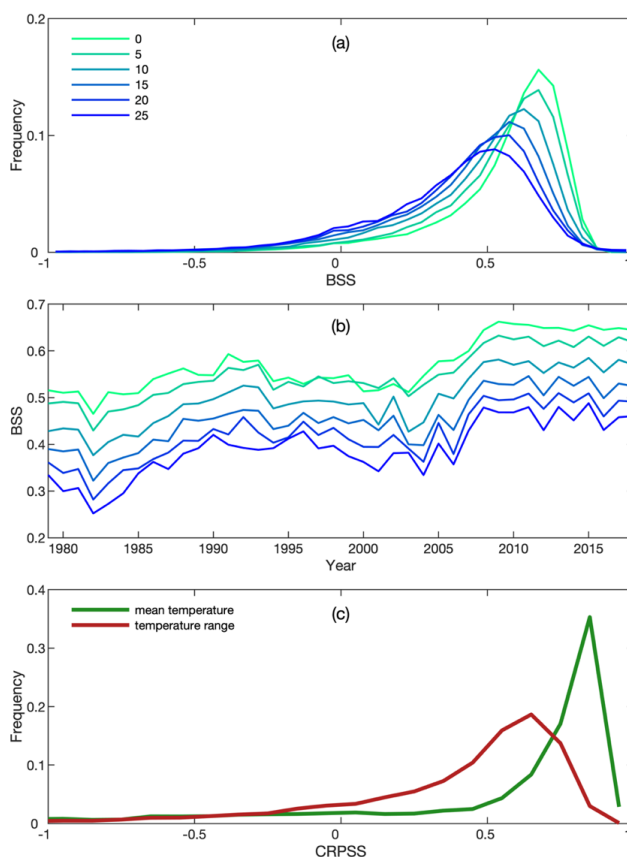
491 Figure 11. The discrimination and reliability diagrams based on ensemble precipitation estimates. Four rain/no rain
492 thresholds (0, 10, 25, 50 mm) are used.

493 The BSS for precipitation and CRPSS for Tmean and Trange are shown in Fig. 12. In most cases, ensemble
494 precipitation shows the highest frequency when BSS is above 0.5. As the precipitation threshold increases, the BSS
495 values decrease. The median BSS values are 0.62, 0.54, and 0.46 for the thresholds of 0, 10, and 20 mm/d, respectively.
496 We note that a small number of cases show BSS values smaller than zero, indicating that the ensemble estimated
497 probability is worse than climatological probability. A low BSS value usually occurs in regions where precipitation is
498 hard to estimate (e.g., Rocky Mountains) resulting in inaccurate parameters of Eq. (1).



499 The BSS for all thresholds shows a clear increasing trend from 1979 to 2018 (Fig. 12b) because the observed
500 precipitation samples from SCDNA increase during this period (Fig. 2 in Tang et al. (2020b)). The increasing trend
501 of BSS is particularly prominent from 2003 to 2009, during which precipitation samples in the USA experience the
502 greatest increase (Tang et al., 2020a). The results show that although infilled station data contribute to higher station
503 densities, observation samples still have a significant effect on gridded data estimation.

504 Tmean shows high CRPSS for most cases with the frequency peak occurring at ~ 0.8 . The CRPSS of Trange is much
505 lower with the peak occurring at ~ 0.6 . The median CRPSS for Tmean and Trange is 0.74 and 0.51, respectively.
506 Analyses show that among stations with negative CRPSS, most are located in Mexico due to the degraded quality of
507 temperature estimates (Sect. 4.1 and 4.2). The long-term variation of CRPSS is not shown because independent
508 temperature stations are insufficient to support validation between 1986 and 2010.



509

510 Figure 12. (a) The frequency distributions of the Brier Skill Score (BSS) for precipitation corresponding to rain/no
511 rain thresholds from 0 to 25 mm/d. (b) The distributions of BSS for precipitation from 1979 to 2018. For each year,



512 the median value of all stations is used. (c) The frequency distributions of the continuous ranked probability skill score
513 (CRPSS) for daily mean temperature and daily temperature range.

514 **5. Discussion**

515 This study presents the framework for producing an ensemble precipitation and temperature dataset over North
516 America. Although we have tested multiple choices of methods (Sect. 3) and overall the product shows good
517 performance (Sect. 4), the methodology still has limitations that need to be improved through continued efforts.

518 **5.1 Implementation of OI**

519 OI is used to merge reanalysis outputs and station data. To implement OI-based merging, a critical step is to estimate
520 the weights. Previous studies usually adopt empirical error or variogram functions and fit the parameters using station
521 observations (e.g., CaPA (Fortin et al., 2015) and CMPA (Shen et al., 2018)); then the parameters are constant for the
522 whole study area in the actual application.

523 In this study, we proposed a novel design, which uses station-based regression estimates as the observation field and
524 calculates weights by directly solving the weight functions based on observation and background errors. Compared
525 with methods that use station data as the observation field, our method is characterized by inferior estimation of the
526 observation field but realistic estimation of weights. The close linkage between the observation field and the weights
527 could benefit OI estimates but comparing different OI implementations is still meaningful and necessary considering
528 OI has been widely used and is the core algorithm of some operational products.

529 Furthermore, regression estimates show worse performance in regions with fewer stations. More advanced
530 interpolation methods that can utilize climatology information and comprehensively consider topographic and
531 atmospheric conditions (Daly et al., 2008; Newman et al., 2019b; Newman and Clark, 2020) should be examined in
532 future studies.

533 **5.2 Probabilistic estimation**

534 Power transformations (e.g., Box-Cox and root/cubic square) with fixed parameters have proven to be useful in
535 precipitation estimation and dataset production (Fortin et al., 2015, 2018; Cornes et al., 2018; Khedhaouiria et al.,
536 2020; Newman et al., 2020). The Box-Cox transformation with a constant parameter is applied following Fortin et al.
537 (2015) and Newman et al. (2019b, 2020). A fixed parameter, however, cannot ensure that transformed precipitation
538 is normally distributed everywhere as is desirable.

539 We tested a series of additional parametric and non-parametric transformations based on power functions, logarithmic
540 functions, or a mix of both, and optimized the parametric transformation functions (including Box-Cox) for every grid
541 by minimizing the objective function which is the sum of squared L-skewness and L-kurtosis (Papalexiou and
542 Koutsoyiannis, 2013). Theoretically, compared to a Box-Cox transformation with a fixed parameter, the optimized



543 functions can obtain precipitation series closer to the normal distribution which should benefit probabilistic estimation,
544 while the evaluation results show that the Box-Cox transformation with a fixed parameter is better at probabilistic
545 estimation than optimized functions. We suggest there are three reasons for this: (1) the standard deviation in Eq. (1)
546 is obtained by interpolating OI errors (Sect. 3.2.2) from neighboring stations, whereas the optimized transformation
547 parameters could be different at those stations, (2) zero precipitation is excluded during optimization to avoid invalid
548 transformation or optimization, which reduces the number of stations for every time step and thus degrades the quality
549 of the spatial interpolation, and (3) the errors caused by back transformation could be large if the optimized
550 transformation is too powerful. More efforts are needed to resolve this problem.

551 There are other potential directions for improvement. For example, SCRF is generated from Gaussian distributions,
552 while other choices such as copulas functions (Papalexiou and Serinaldi, 2020) show potential in probabilistic
553 estimation. The spatial correlation length is constant for the whole study area following Newman et al. (2015, 2019b),
554 which may introduce uncertainties for a large domain. Overall, studies related to the production of ensemble
555 meteorological datasets are still insufficient, particularly for large areas. More studies are needed to clarify the critical
556 issues in large-scale probabilistic estimation and explore the effect of parameter/method choices on probabilistic
557 estimates.

558 **5.3 Alternate data sources**

559 The quality of source data (station observations and reanalysis models) primarily determines the quality of output
560 datasets. The density of stations has a critical effect on the accuracy of the observation field and probabilistic estimates.
561 While SCDNA collects data from multiple datasets, efforts are ongoing to expand the database by involving station
562 sources such as provincial station networks in Canada.

563 For reanalysis products, ERA5, MERRA-2, and JRA-55 are regridded using locally weighted linear regression to meet
564 the target resolution. There are some choices for future improvement, such as (1) adopting/developing better
565 downscaling methods or (2) utilizing outputs from high-resolution re-analysis products or forecasting models such as
566 ERA5-Land or the Weather Research and Forecasting (WRF) model. For the latter one, a comprehensive assessment
567 of available products is necessary before substituting the three reanalysis products used by EMDNA. Moreover,
568 including other data sources such as satellite (e.g. GPM-IMERG) and weather radar estimates is also an opportunity.

569 **5.4 Precipitation under-catch**

570 Although station precipitation observations are used as the reference in this study, these values are subject to
571 measurement errors such as wetting loss, wind-induced under-catch, and trace precipitation. Under-catch of
572 precipitation is particularly severe in high latitudes and mountains due to the stronger wind and frequent snowfall
573 (Sevruk, 1984; Goodison et al., 1998; Nešpor and Sevruk, 1999; Yang et al., 2005; Scaff et al., 2015; Kochendorfer
574 et al., 2018). For example, underestimation of precipitation could be larger than 100% in Alaska (Yang et al., 1998).
575 Bias correction of station precipitation data should consider many factors such as gauge types, precipitation phase,



576 and environmental conditions, which would be very complicated when a large number of sparsely distributed stations
577 are involved over the whole of North America.

578 The under-catch correction used in this study relies on bias-corrected precipitation climatology produced by Beck et
579 al. (2020), which infers the long-term precipitation using a Budyko curve and streamflow observations. The bias-
580 corrected precipitation climatology, however, is less accurate in northern Canada where streamflow stations are few
581 (Beck et al., 2020). In addition, the streamflow data used by the bias-corrected climatology also contain uncertainties
582 (Hamilton and Moore, 2012; Kiang et al., 2018) related to factors such as streamflow derivation methods (e.g., rate
583 curves) and measurement instruments. Whilst various under-catch correction methods (e.g., Fuchs et al., 2001; Beck
584 et al., 2020; Newman et al., 2020) exist, further studies are needed to compare these solutions considering their
585 effectiveness and availability of input data in a large domain.

586 **6. Data availability**

587 The EMDNA dataset is available at <https://doi.org/10.20383/101.0275> (Tang et al., 2020a) in netCDF format.
588 Individual ensemble member, ensemble mean, and ensemble spread of precipitation, Tmean, and Trange are provided.
589 The total data size is 3.35 TB. Since the 100 members are equally plausible, users can download fewer members if the
590 storage space and processing time are limited.

591 The deterministic OI estimates of precipitation, PoP, Tmean, and Trange produced in this study are also available in
592 netCDF format. The high-quality OI estimates merge reanalysis and station data, which can be useful to applications
593 that do not need ensemble forcings. The total data size is 40.84 GB.

594 A teaser dataset of probabilistic estimates is provided to facilitate easy preview of EMDNA without downloading the
595 entire dataset. The teaser dataset covers the region from -116.8° to -115.2°W, and 50.7° to 51.9°N, the time from 2014
596 to 2015, and the ensemble members from 1 to 25. The total data size is smaller than 30 MB. See Appendix E for a
597 brief introduction.

598 **7. Summary and Conclusions**

599 Ensemble meteorological datasets are of great value to hydrological and meteorological studies. Given the lack of a
600 historical ensemble dataset for the entire North America, this study develops EMDNA by integrating multi-source
601 information to overcome the limitation of sparse stations in high-latitude regions. EMDNA contains precipitation,
602 Tmean, and Trange estimates at 0.1° spatial resolution and daily temporal resolution from 1979 to 2018 with 100
603 members. Multiple methodological choices are examined when determining critical steps in the production of
604 EMDNA. The ultimate framework composes of four main steps: (1) generating station-based interpolation estimates
605 from SCDNA using locally weighted linear/logistic regression, (2) regridding, correction, and merging of reanalysis
606 products (ERA5, MERRA-2, and JRA-55), (3) merging station-reanalysis estimates using OI based on a novel method



607 of OI weight calculation, and (4) generating ensemble estimates by sampling from the estimated probability
608 distributions with the perturbations provided by SCRF.

609 The performance of each step is comprehensively evaluated using multiple methods. The results show that the design
610 of the framework is effective. In short, we find that (1) station-based interpolation estimates are less accurate in regions
611 with sparse stations (e.g., high latitudes) and complex terrain; (2) BMA-merged reanalysis estimates show notable
612 improvement against raw reanalysis estimates, particularly for precipitation and Trange and over high-latitude regions;
613 (3) OI achieves more accurate estimates than interpolation and reanalysis estimates from (1) and (2), respectively, and
614 the complementary effect between reanalysis and interpolation estimates contributes to the large improvement of OI
615 estimates in sparsely gauged regions; and (4) ensemble precipitation estimates show good discrimination and
616 reliability performance for all thresholds, and the BSS values for ensemble precipitation and CRPSS values for
617 ensemble Tmean and Trange are high in most cases. BSS values of ensemble precipitation increase from 1979 to 2018
618 due to the increase of the number of stations.

619 Overall, EMDNA (version 1) will be useful for many applications in North America such as regional or continental
620 hydrological modeling. Meanwhile, we recognize that the current framework is not perfect and have provided
621 suggestions on the future directions for large-scale ensemble estimation of meteorological variables. Continuing
622 efforts from the community are needed to promote the development of probabilistic estimation methods and datasets.

623

624 **Author contributions:** GT and MC designed the framework of this study. GT collected data, performed the analyses
625 and wrote the paper. MC, SP, AN and AW contributed to the design of the methodology and result evaluation. SP,
626 DB and PW contributed to the evaluation of methodology and results. All authors contributed to data analysis,
627 discussions about the methods and results, and paper improvement.

628 **Competing interests:** The authors declare that they have no conflict of interest.

629 **Acknowledgment:** The study is funded by the Global Water Futures (GWF) program in Canada. The authors
630 appreciate the extensive efforts from the developers of the ground and reanalysis datasets to make their products
631 available. The authors also thank Federated Research Data Repository (FRDR; <https://www.frdr-dfdr.ca>; Access Date:
632 September 29, 2020) for publishing our dataset as open access to users.

633

634 **Appendix A. Regression coefficients**

635 The coefficients for locally weight linear regression are estimated using weighted least square. Given a station i with
636 m neighboring stations, let $\mathbf{A} = [1, A_1, \dots, A_n]$ be the $m \times n + 1$ attribute matrix, let $\mathbf{x} = (x_1, x_2, \dots, x_m)$ be the station
637 observations from neighboring stations, and let $\mathbf{w}_i = (w_{i,1}, w_{i,2}, \dots, w_{i,m})$ be the weight vector with distance-based



638 weights computed from Eq. (5). The regression coefficients $\boldsymbol{\beta} = (\beta_0, \beta_1, \dots, \beta_n)$ for Eq. (4) are estimated from the
639 weighted normal equation as

$$\boldsymbol{\beta} = (\mathbf{A}^T \mathbf{W} \mathbf{A})^{-1} \mathbf{A}^T \mathbf{W} \mathbf{x}, \quad \text{A1}$$

640 where the $m \times m$ weight matrix $\mathbf{W} = \mathbf{I}_m \mathbf{w}_i$ is a diagonal matrix obtained by multiplying the $m \times m$ identity matrix
641 \mathbf{I}_m with the weight vector \mathbf{w}_i .

642 The regression coefficients for logistic regression (Eq. 6) are estimated iteratively as:

$$\boldsymbol{\beta}^{new} = \boldsymbol{\beta}^{old} + (\mathbf{A}^T \mathbf{W} \mathbf{V} \mathbf{A})^{-1} \mathbf{A}^T \mathbf{W} (\mathbf{P}_0 - \boldsymbol{\pi}) \quad \text{A2}$$

$$\boldsymbol{\pi} = \frac{1}{1 + \exp(-\mathbf{A} \boldsymbol{\beta}^{old})} \quad \text{A3}$$

$$\mathbf{V} = \mathbf{I}_m \boldsymbol{\pi} (1 - \boldsymbol{\pi}) \quad \text{A4}$$

643 where \mathbf{P}_0 is a vector of binary precipitation occurrence for neighboring stations, $\boldsymbol{\pi}$ is the vector of estimated PoP for
644 neighboring stations, and \mathbf{V} is the diagonal variance matrix for PoP. The regression coefficients $\boldsymbol{\beta}^{old}$ are initialized as
645 a vector of ones.

646

647 **Appendix B. Anomalous stations**

648 To exclude climatologically anomalous stations, for temperature (Tmean or Trange), we calculate: (1) the absolute
649 difference of the climatological mean between the target station and the average value of its 10 neighboring stations
650 (referred as Diff-1), and (2) the absolute difference of the climatological mean between station observation and
651 regression estimates (referred as Diff-2). A temperature station will be excluded if its Diff-1 is larger than the 95%
652 percentile and its Diff-2 larger than the 99% percentile of all stations simultaneously. The threshold of percentiles for
653 Diff-1 is lower to better identify some climatologically anomalous stations.

654 For precipitation, the ratio (Ratio-1 and Ratio-2) is obtained in the same way with the Diff-1 and Diff-2 of temperature.
655 A two-tailed check is used for precipitation compared with the one-tailed check for temperature. A precipitation station
656 will be excluded if its Ratio-1 is larger (or smaller) than the 99.9% (1%) percentile and its Ratio-2 larger (or smaller)
657 than the 99.9% (1%) percentile simultaneously. This check has more tolerance for heavy precipitation but tries to
658 exclude more extremely dry stations.



659 As a result, ~1.5% precipitation and temperature stations are rejected, after which algorithms described in Sect. 3.1.1
660 and 3.1.2 are re-run. Stations can be anomalous because they are badly operated or simply because they are unique in
661 terms of topography or climate. The usage of Diff-2 or Ratio-2 is helpful to avoid excluding unique stations, but for
662 cases where the regression is ineffective, the unique stations can still be wrongly excluded. Although the effect on
663 final estimates could be rather small, better strategies could be used in future studies.

664

665 **Appendix C. Error of BMA-merged reanalysis estimates**

666 The errors of BMA-merged estimates are first estimated for all stations and then interpolated to grids. Considering
667 station observations cannot be used to evaluate merged estimates once they are used in bias correction or BMA weight
668 estimation, a two-layer cross-validation strategy is designed. In the first layer, we treat i as the target station and find
669 its m ($j_1 = 1, 2, \dots, m; i \notin j_1$) neighboring stations. In the second layer, we treat each j_1 as a target station, and (1)
670 find m ($j_2 = 1, 2, \dots, m; i \notin j_2$) neighboring stations for each j_1 , (2) calculate linear scaling correction factors for all
671 j_2 , (3) estimate the correction factor for the target j_1 by interpolating factors at all j_2 stations using inverse distance
672 weighting, (4) correct estimates at j_1 using the correction factor, (5) calculate BMA weights of three reanalysis
673 products for all j_1 stations, (6) interpolate BMA weights from all j_1 stations to the target station i and merge the three
674 reanalysis products for i , and (7) calculate the difference between merged reanalysis estimates and station observations
675 for i . This two-layer design may seem convoluted but is necessary to ensure that the error estimation is realistic. j_1
676 and j_2 could be partly overlapped due to their close locations but should not cause a large effect on the error estimation
677 for i because data for i are only used in (7) in this design. The station-based errors are interpolated to all grids using
678 inverse distance weighting.

679 **Appendix D. Metrics for probabilistic evaluation**

680 BSS is calculated based on the Brier Score (BS):

$$\text{BSS} = 1 - \frac{\text{BS}}{\text{BS}_{\text{clim}}} \quad \text{D1}$$

$$\text{BS} = \frac{1}{n} \sum_{i=1}^n (\text{PoP}_{\text{ens}} - \text{PoP}_{\text{obs}})^2 \quad \text{D2}$$

681 where PoP_{ens} is the estimated probability of ensemble precipitation, PoP_{obs} is the observed binary precipitation
682 occurrence, n is the sample number, and BS_{clim} is the climatological BS by assigning the climatological probability
683 to all samples. When the two series match the value of BSS will be equal to one.

684 CRPS is calculated based on the continuous ranked probability skill score (CRPS; Hersbach, 2000):



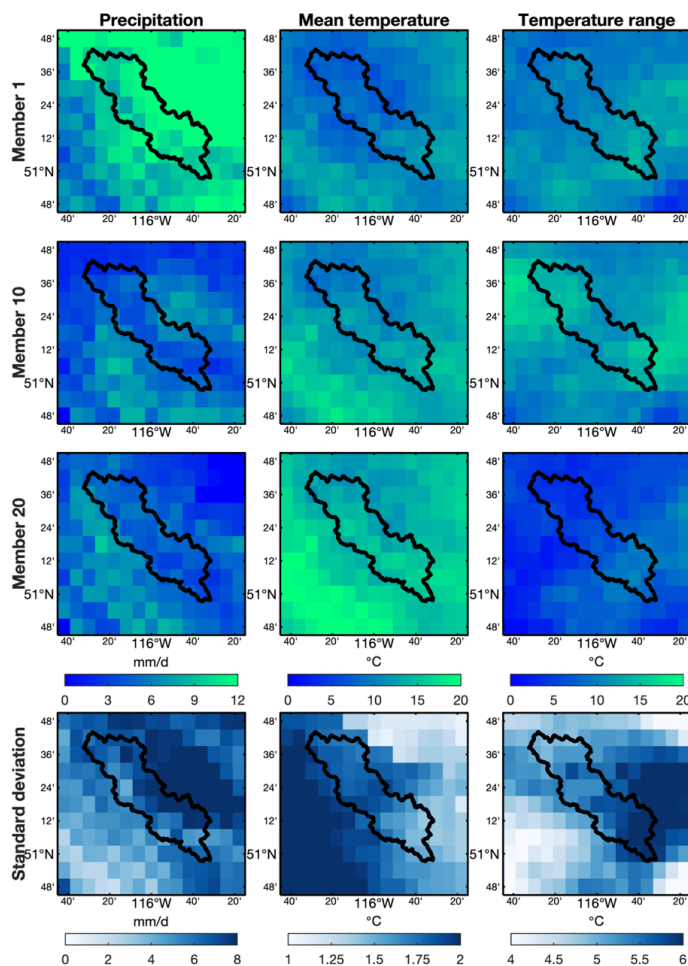
$$\text{CRPSS} = 1 - \frac{\text{CRPS}}{\text{CRPS}_{\text{clim}}} \quad \text{D3}$$

$$\text{CRPS} = \int_{-\infty}^{\infty} (F(x) - H(x \geq x_o))^2 dx \quad \text{D4}$$

685 where $F(x)$ is the CDF of the ensemble temperature estimate x , x_o is the observed temperature, $H(x \geq x_o)$ is the
686 Heaviside step function with the value being one if the condition $x \geq x_o$ is satisfied and zero if not satisfied, and
687 $\text{CRPS}_{\text{clim}}$ is the climatological CPRS. CRPS measures the distance between the CDF of probabilistic estimates and
688 observations. For a perfect match, the value of CRPSS would be one.

689 **Appendix E. Teaser dataset**

690 The teaser dataset is a subset of EMDNA probabilistic estimates for a small region (-116.8° to -115.2°W, 50.7° to
691 51.9°N) and a short period (2014 to 2015) with only 25 ensemble members. Users can easily download and preview
692 the teaser dataset (<30 MB) before downloading the entire EMDNA dataset (~3 TB or ~40 GB) as shown in Sect. 6.
693 The region covers the Bow River basin above Banff, Canada, which is located in the Canadian Rockies (Figure A1).
694 The spread of ensemble members in this region could be large due to the complex topography and limited stations.



695

696 Figure A1. The distributions of daily precipitation (the first column), mean daily temperature (the second column),
697 and daily temperature range (the third column) on 29 June 2015. The first to third rows represent ensemble members
698 1, 10, and 20, respectively. The fourth row represents the standard deviation of 25 members for this day. The black
699 line outlines the Bow River basin above Banff, Canada.

700

701 References

- 702 Aalto, J., Pirinen, P. and Jylhä, K.: New gridded daily climatology of Finland: Permutation-based uncertainty estimates
703 and temporal trends in climate, *J. Geophys. Res. Atmospheres*, 121(8), 3807–3823, doi:10.1002/2015JD024651, 2016.
- 704 Adler, R. F., Gu, G. J., Sapiano, M., Wang, J. J. and Huffman, G. J.: Global Precipitation: Means, Variations and
705 Trends During the Satellite Era (1979-2014), *Surv. Geophys.*, 38(4), 679–699, doi:10.1007/s10712-017-9416-4, 2017.



- 706 Arias-Hidalgo, M., Bhattacharya, B., Mynett, A. E. and van Griensven, A.: Experiences in using the TMPA-3B42R
707 satellite data to complement rain gauge measurements in the Ecuadorian coastal foothills, *Hydrol. Earth Syst. Sci.*,
708 17(7), 2905–2915, doi:10.5194/hess-17-2905-2013, 2013.
- 709 Beck, H. E., Vergopolan, N., Pan, M., Levizzani, V., van Dijk, A. I. J. M., Weedon, G., Brocca, L., Pappenberger, F.,
710 Huffman, G. J. and Wood, E. F.: Global-scale evaluation of 23 precipitation datasets using gauge observations and
711 hydrological modeling, *Hydrol. Earth Syst. Sci.*, 21(12), 6201–6217, doi:10.5194/hess-2017-508, 2017.
- 712 Beck, H. E., Wood, E. F., Pan, M., Fisher, C. K., Miralles, D. G., van Dijk, A. I. J. M., McVicar, T. R. and Adler, R.
713 F.: MSWEP V2 Global 3-Hourly 0.1° Precipitation: Methodology and Quantitative Assessment, *Bull. Am. Meteorol.*
714 *Soc.*, 100(3), 473–500, doi:10.1175/BAMS-D-17-0138.1, 2019.
- 715 Beck, H. E., Wood, E. F., McVicar, T. R., Zambrano-Bigiarini, M., Alvarez-Garreton, C., Baez-Villanueva, O. M.,
716 Sheffield, J. and Karger, D. N.: Bias Correction of Global High-Resolution Precipitation Climatologies Using
717 Streamflow Observations from 9372 Catchments, *J. Clim.*, 33(4), 1299–1315, doi:10.1175/JCLI-D-19-0332.1, 2020.
- 718 Brier, G. W.: Verification of forecasts expressed in terms of probability, *Mon. Weather Rev.*, 78(1), 1–3,
719 doi:10.1175/1520-0493(1950)078<0001:VOFEIT>2.0.CO;2, 1950.
- 720 Caillouet, L., Vidal, J.-P., Sauquet, E., Graff, B. and Soubeyroux, J.-M.: SCOPE Climate: a 142-year daily high-
721 resolution ensemble meteorological reconstruction dataset over France, *Earth Syst. Sci. Data*, 11(1), 241–260,
722 doi:https://doi.org/10.5194/essd-11-241-2019, 2019.
- 723 Cannon, A. J., Sobie, S. R. and Murdock, T. Q.: Bias Correction of GCM Precipitation by Quantile Mapping: How
724 Well Do Methods Preserve Changes in Quantiles and Extremes?, *J. Clim.*, 28(17), 6938–6959, doi:10.1175/JCLI-D-
725 14-00754.1, 2015.
- 726 Chen, Y., Yuan, W., Xia, J., Fisher, J. B., Dong, W., Zhang, X., Liang, S., Ye, A., Cai, W. and Feng, J.: Using Bayesian
727 model averaging to estimate terrestrial evapotranspiration in China, *J. Hydrol.*, 528, 537–549,
728 doi:10.1016/j.jhydrol.2015.06.059, 2015.
- 729 Clark, M. P. and Slater, A. G.: Probabilistic Quantitative Precipitation Estimation in Complex Terrain, *J.*
730 *Hydrometeorol.*, 7(1), 3–22, doi:10.1175/JHM474.1, 2006.
- 731 Clark, M. P., Slater, A. G., Barrett, A. P., Hay, L. E., McCabe, G. J., Rajagopalan, B. and Leavesley, G. H.:
732 Assimilation of snow covered area information into hydrologic and land-surface models, *Adv. Water Resour.*, 29(8),
733 1209–1221, doi:10.1016/j.advwatres.2005.10.001, 2006.
- 734 Cornes, R. C., Schrier, G. van der, Besselaar, E. J. M. van den and Jones, P. D.: An ensemble version of the E-OBS
735 temperature and precipitation data sets, *J. Geophys. Res. Atmospheres*, 123(17), 9391–9409,
736 doi:10.1029/2017JD028200, 2018.
- 737 Daly, C., Halbleib, M., Smith, J. I., Gibson, W. P., Doggett, M. K., Taylor, G. H., Curtis, J. and Pasteris, P. P.:
738 Physiographically sensitive mapping of climatological temperature and precipitation across the conterminous United
739 States, *Int. J. Climatol.*, 28(15), 2031–2064, doi:10.1002/joc.1688, 2008.
- 740 Di Luzio, M., Johnson, G. L., Daly, C., Eischeid, J. K. and Arnold, J. G.: Constructing Retrospective Gridded Daily
741 Precipitation and Temperature Datasets for the Conterminous United States, *J. Appl. Meteorol. Climatol.*, 47(2), 475–
742 497, doi:10.1175/2007JAMC1356.1, 2008.
- 743 Dinku, T., Anagnostou, E. N. and Borga, M.: Improving radar-based estimation of rainfall over complex terrain, *J.*
744 *Appl. Meteorol.*, 41(12), 1163–1178, 2002.



- 745 Donat, M. G., Sillmann, J., Wild, S., Alexander, L. V., Lippmann, T. and Zwiers, F. W.: Consistency of Temperature
746 and Precipitation Extremes across Various Global Gridded In Situ and Reanalysis Datasets, *J. Clim.*, 27(13), 5019–
747 5035, doi:10.1175/JCLI-D-13-00405.1, 2014.
- 748 Duan, Q. and Phillips, T. J.: Bayesian estimation of local signal and noise in multimodel simulations of climate change,
749 *J. Geophys. Res. Atmospheres*, 115(D18), doi:10.1029/2009JD013654, 2010.
- 750 Duan, S.-B. and Li, Z.-L.: Spatial Downscaling of MODIS Land Surface Temperatures Using Geographically
751 Weighted Regression: Case Study in Northern China, *IEEE Trans. Geosci. Remote Sens.*, 54(11), 6458–6469,
752 doi:10.1109/TGRS.2016.2585198, 2016.
- 753 Eischeid, J. K., Pasteris, P. A., Diaz, H. F., Plantico, M. S. and Lott, N. J.: Creating a Serially Complete, National
754 Daily Time Series of Temperature and Precipitation for the Western United States, *J. Appl. Meteorol.*, 39(9), 1580–
755 1591, doi:10.1175/1520-0450(2000)039<1580:CASCND>2.0.CO;2, 2000.
- 756 Fick, S. E. and Hijmans, R. J.: WorldClim 2: new 1-km spatial resolution climate surfaces for global land areas, *Int.*
757 *J. Climatol.*, 37(12), 4302–4315, 2017.
- 758 Fortin, V., Roy, G., Donaldson, N. and Mahidjiba, A.: Assimilation of radar quantitative precipitation estimations in
759 the Canadian Precipitation Analysis (CaPA), *J. Hydrol.*, 531, 296–307, doi:10.1016/j.jhydrol.2015.08.003, 2015.
- 760 Fortin, V., Roy, G., Stadnyk, T., Koenig, K., Gasset, N. and Mahidjiba, A.: Ten Years of Science Based on the
761 Canadian Precipitation Analysis: A CaPA System Overview and Literature Review, *Atmosphere-Ocean*, 56(3), 178–
762 196, doi:10.1080/07055900.2018.1474728, 2018.
- 763 Frei, C. and Isotta, F. A.: Ensemble Spatial Precipitation Analysis From Rain Gauge Data: Methodology and
764 Application in the European Alps, *J. Geophys. Res. Atmospheres*, 124(11), 5757–5778, doi:10.1029/2018JD030004,
765 2019.
- 766 Fuchs, T., Rapp, J., Rubel, F. and Rudolf, B.: Correction of synoptic precipitation observations due to systematic
767 measuring errors with special regard to precipitation phases, *Phys. Chem. Earth Part B Hydrol. Oceans Atmosphere*,
768 26(9), 689–693, 2001.
- 769 Funk, C., Peterson, P., Landsfeld, M., Pedreros, D., Verdin, J., Shukla, S., Husak, G., Rowland, J., Harrison, L., Hoell,
770 A. and Michaelsen, J.: The climate hazards infrared precipitation with stations--a new environmental record for
771 monitoring extremes, *Sci. Data*, 2, 150066, doi:10.1038/sdata.2015.66, 2015.
- 772 Gelaro, R., McCarty, W., Suárez, M. J., Todling, R., Molod, A., Takacs, L., Randles, C. A., Darmenov, A., Bosilovich,
773 M. G., Reichle, R., Wargan, K., Coy, L., Cullather, R., Draper, C., Akella, S., Buchard, V., Conaty, A., da Silva, A.
774 M., Gu, W., Kim, G.-K., Koster, R., Lucchesi, R., Merkova, D., Nielsen, J. E., Partyka, G., Pawson, S., Putman, W.,
775 Rienecker, M., Schubert, S. D., Sienkiewicz, M. and Zhao, B.: The Modern-Era Retrospective Analysis for Research
776 and Applications, Version 2 (MERRA-2), *J. Clim.*, 30(14), 5419–5454, doi:10.1175/jcli-d-16-0758.1, 2017.
- 777 Goodison, B. E., Louie, P. Y. and Yang, D.: WMO solid precipitation measurement intercomparison, 1998.
- 778 Habib, E., Haile, A. T., Sazib, N., Zhang, Y. and Rientjes, T.: Effect of Bias Correction of Satellite-Rainfall Estimates
779 on Runoff Simulations at the Source of the Upper Blue Nile, *Remote Sens.*, 6(7), 6688–6708, doi:10.3390/rs6076688,
780 2014.
- 781 Hamilton, A. S. and Moore, R. D.: Quantifying Uncertainty in Streamflow Records, *Can. Water Resour. J. Rev. Can.*
782 *Ressour. Hydr.*, 37(1), 3–21, doi:10.4296/cwrj3701865, 2012.
- 783 Harris, I., Osborn, T. J., Jones, P. and Lister, D.: Version 4 of the CRU TS monthly high-resolution gridded
784 multivariate climate dataset, *Sci. Data*, 7(1), 109, doi:10.1038/s41597-020-0453-3, 2020.



- 785 Haylock, M. R., Hofstra, N., Klein Tank, A. M. G., Klok, E. J., Jones, P. D. and New, M.: A European daily high-
786 resolution gridded data set of surface temperature and precipitation for 1950–2006, *J. Geophys. Res. Atmospheres*,
787 113(D20), doi:10.1029/2008JD010201, 2008.
- 788 Hellinger, E.: Neue begründung der theorie quadratischer formen von unendlichvielen veränderlichen., *J. Für Reine*
789 *Angew. Math. Crelles J.*, 1909(136), 210–271, 1909.
- 790 Hempel, S., Frieler, K., Warszawski, L., Schewe, J. and Piontek, F.: A trend-preserving bias correction – the
791 ISI-MIP approach, *Earth Syst. Dyn.*, 4(2), 219–236, doi:10.5194/esd-4-219-2013, 2013.
- 792 Henn, B., Newman, A. J., Livneh, B., Daly, C. and Lundquist, J. D.: An assessment of differences in gridded
793 precipitation datasets in complex terrain, *J. Hydrol.*, 556, 1205–1219, doi:10.1016/j.jhydrol.2017.03.008, 2018.
- 794 Herrnegger, M., Senoner, T. and Nachtnebel, H.-P.: Adjustment of spatio-temporal precipitation patterns in a high
795 Alpine environment, *J. Hydrol.*, 556, 913–921, doi:10.1016/j.jhydrol.2016.04.068, 2018.
- 796 Hersbach, H.: Decomposition of the continuous ranked probability score for ensemble prediction systems, *Weather*
797 *Forecast.*, 15(5), 559–570, 2000.
- 798 Hersbach, H., Bell, B., Berrisford, P., Hirahara, S., Horányi, A., Muñoz-Sabater, J., Nicolas, J., Peubey, C., Radu, R.,
799 Schepers, D., Simmons, A., Soci, C., Abdalla, S., Abellan, X., Balsamo, G., Bechtold, P., Biavati, G., Bidlot, J.,
800 Bonavita, M., Chiara, G. D., Dahlgren, P., Dee, D., Diamantakis, M., Dragani, R., Flemming, J., Forbes, R., Fuentes,
801 M., Geer, A., Haimberger, L., Healy, S., Hogan, R. J., Hólm, E., Janisková, M., Keeley, S., Laloyaux, P., Lopez, P.,
802 Lupu, C., Radnoti, G., Rosnay, P. de, Rozum, I., Vamborg, F., Villaume, S. and Thépaut, J.-N.: The ERA5 global
803 reanalysis, *Q. J. R. Meteorol. Soc.*, 146(730), 1999–2049, doi:10.1002/qj.3803, 2020.
- 804 Hoeting, J. A., Madigan, D., Raftery, A. E. and Volinsky, C. T.: Bayesian Model Averaging: A Tutorial, *Stat. Sci.*,
805 14(4), 382–401, 1999.
- 806 Hong, Y., Hsu, K., Moradkhani, H. and Sorooshian, S.: Uncertainty quantification of satellite precipitation estimation
807 and Monte Carlo assessment of the error propagation into hydrologic response, *Water Resour. Res.*, 42(8),
808 doi:10.1029/2005wr004398, 2006.
- 809 Hu, Q., Li, Z., Wang, L., Huang, Y., Wang, Y. and Li, L.: Rainfall Spatial Estimations: A Review from Spatial
810 Interpolation to Multi-Source Data Merging, *Water*, 11(3), 579, doi:10.3390/w11030579, 2019.
- 811 Huffman, G. J., Bolvin, D. T., Nelkin, E. J., Wolff, D. B., Adler, R. F., Gu, G., Hong, Y., Bowman, K. P. and Stocker,
812 E. F.: The TRMM Multisatellite Precipitation Analysis (TMPA): Quasi-Global, Multiyear, Combined-Sensor
813 Precipitation Estimates at Fine Scales, *J. Hydrometeorol.*, 8(1), 38–55, doi:10.1175/jhm560.1, 2007.
- 814 Karger, D. N., Conrad, O., Bohner, J., Kawohl, T., Kreft, H., Soria-Auza, R. W., Zimmermann, N. E., Linder, H. P.
815 and Kessler, M.: Climatologies at high resolution for the earth’s land surface areas, *Sci Data*, 4, 170122,
816 doi:10.1038/sdata.2017.122, 2017.
- 817 Kemp, W. P., Burnell, D. G., Everson, D. O. and Thomson, A. J.: Estimating Missing Daily Maximum and Minimum
818 Temperatures, *J. Clim. Appl. Meteorol.*, 22(9), 1587–1593, doi:10.1175/1520-
819 0450(1983)022<1587:EMDMAM>2.0.CO;2, 1983.
- 820 Khedhaouria, D., Bélair, S., Fortin, V., Roy, G. and Lespinas, F.: High Resolution (2.5km) Ensemble Precipitation
821 Analysis across Canada, *J. Hydrometeorol.*, doi:10.1175/JHM-D-19-0282.1, 2020.
- 822 Kiang, J. E., Gazoorian, C., McMillan, H., Coxon, G., Coz, J. L., Westerberg, I. K., Belleville, A., Sevrez, D., Sikorska,
823 A. E., Petersen-Øverleir, A., Reitan, T., Freer, J., Renard, B., Mansanarez, V. and Mason, R.: A Comparison of
824 Methods for Streamflow Uncertainty Estimation, *Water Resour. Res.*, 54(10), 7149–7176,
825 doi:10.1029/2018WR022708, 2018.



- 826 Kirstetter, P.-E., Gourley, J. J., Hong, Y., Zhang, J., Moazamigoodarzi, S., Langston, C. and Arthur, A.: Probabilistic
827 precipitation rate estimates with ground-based radar networks, *Water Resour. Res.*, 51(3), 1422–1442,
828 doi:10.1002/2014WR015672, 2015.
- 829 Kobayashi, S., Ota, Y., Harada, Y., Ebata, A., Moriya, M., Onoda, H., Onogi, K., Kamahori, H., Kobayashi, C., Endo,
830 H., Miyaoka, K. and Takahashi, K.: The JRA-55 Reanalysis: General Specifications and Basic Characteristics, *J.*
831 *Meteorol. Soc. Jpn. Ser II*, 93(1), 5–48, doi:10.2151/jmsj.2015-001, 2015.
- 832 Kochendorfer, J., Nitu, R., Wolff, M., Mekis, E., Rasmussen, R., Baker, B., Earle, M. E., Reverdin, A., Wong, K.,
833 Smith, C. D., Yang, D., Roulet, Y.-A., Meyers, T., Buisan, S., Isaksen, K., Brækkan, R., Landolt, S. and Jachcik, A.:
834 Testing and development of transfer functions for weighing precipitation gauges in WMO-SPICE, *Hydrol. Earth Syst.*
835 *Sci.*, 22(2), 1437–1452, doi:https://doi.org/10.5194/hess-22-1437-2018, 2018.
- 836 Lader, R., Bhatt, U. S., Walsh, J. E., Rupp, T. S. and Bieniek, P. A.: Two-Meter Temperature and Precipitation from
837 Atmospheric Reanalysis Evaluated for Alaska, *J. Appl. Meteorol. Climatol.*, 55(4), 901–922, doi:10.1175/JAMC-D-
838 15-0162.1, 2016.
- 839 Livneh, B., Rosenberg, E. A., Lin, C., Nijssen, B., Mishra, V., Andreadis, K. M., Maurer, E. P. and Lettenmaier, D.
840 P.: A Long-Term Hydrologically Based Dataset of Land Surface Fluxes and States for the Conterminous United States:
841 Update and Extensions, *J. Clim.*, 26(23), 9384–9392, doi:10.1175/JCLI-D-12-00508.1, 2013.
- 842 Lu, X., Tang, G., Wang, X., Liu, Y., Wei, M. and Zhang, Y.: The Development of a Two-Step Merging and
843 Downscaling Method for Satellite Precipitation Products, *Remote Sens.*, 12(3), 398, 2020.
- 844 Ma, Y., Yang, Y., Han, Z., Tang, G., Maguire, L., Chu, Z. and Hong, Y.: Comprehensive evaluation of Ensemble
845 Multi-Satellite Precipitation Dataset using the Dynamic Bayesian Model Averaging scheme over the Tibetan plateau,
846 *J. Hydrol.*, 556, 634–644, doi:10.1016/j.jhydrol.2017.11.050, 2018a.
- 847 Ma, Y., Hong, Y., Chen, Y., Yang, Y., Tang, G., Yao, Y., Long, D., Li, C., Han, Z. and Liu, R.: Performance of
848 Optimally Merged Multisatellite Precipitation Products Using the Dynamic Bayesian Model Averaging Scheme Over
849 the Tibetan Plateau, *J. Geophys. Res. Atmospheres*, 123(2), 814–834, doi:10.1002/2017jd026648, 2018b.
- 850 Ma, Z., Xu, J., Zhu, S., Yang, J., Tang, G., Yang, Y., Shi, Z. and Hong, Y.: AIMERG: a new Asian precipitation
851 dataset (0.1°/half-hourly, 2000–2015) by calibrating the GPM-era IMERG at a daily scale using APHRODITE, *Earth*
852 *Syst. Sci. Data*, 12(3), 1525–1544, doi:https://doi.org/10.5194/essd-12-1525-2020, 2020.
- 853 Mahfouf, J.-F., Brasnett, B. and Gagnon, S.: A Canadian precipitation analysis (CaPA) project: Description and
854 preliminary results, *Atmosphere–Ocean*, 45(1), 1–17, doi:10.3137/ao.v450101, 2007.
- 855 Maurer, E. P., Wood, A. W., Adam, J. C., Lettenmaier, D. P. and Nijssen, B.: A Long-Term Hydrologically Based
856 Dataset of Land Surface Fluxes and States for the Conterminous United States, *J. Clim.*, 15, 15, 2002.
- 857 Mears, C. A., Wentz, F. J., Thorne, P. and Bernie, D.: Assessing uncertainty in estimates of atmospheric temperature
858 changes from MSU and AMSU using a Monte-Carlo estimation technique, *J. Geophys. Res. Atmospheres*, 116(D8),
859 doi:10.1029/2010JD014954, 2011.
- 860 Mendoza, P. A., Wood, A. W., Clark, E. A., Rothwell, E., Clark, M. P., Nijssen, B., Brekke, L. D. and Arnold, J. R.:
861 An intercomparison of approaches for improving predictability in operational seasonal streamflow forecasting, *Hydrol*
862 *Earth Syst Sci Discuss*, 2017.
- 863 Mooney, P. A., Mulligan, F. J. and Fealy, R.: Comparison of ERA-40, ERA-Interim and NCEP/NCAR reanalysis data
864 with observed surface air temperatures over Ireland, *Int. J. Climatol.*, 31(4), 545–557, doi:10.1002/joc.2098, 2011.



- 865 Morice, C. P., Kennedy, J. J., Rayner, N. A. and Jones, P. D.: Quantifying uncertainties in global and regional
866 temperature change using an ensemble of observational estimates: The HadCRUT4 data set, *J. Geophys. Res.*
867 *Atmospheres*, 117(D8), doi:10.1029/2011JD017187, 2012.
- 868 Nešpor, V. and Sevruk, B.: Estimation of Wind-Induced Error of Rainfall Gauge Measurements Using a Numerical
869 Simulation, *J. Atmospheric Ocean. Technol.*, 16(4), 450–464, doi:10.1175/1520-
870 0426(1999)016<0450:EOWIEO>2.0.CO;2, 1999.
- 871 Newman, A. J. and Clark, M. P.: TIER version 1.0: an open-source Topographically InformEd Regression (TIER)
872 model to estimate spatial meteorological fields, *Geosci. Model Dev.*, 13(4), 1827–1843,
873 doi:https://doi.org/10.5194/gmd-13-1827-2020, 2020.
- 874 Newman, A. J., Clark, M. P., Craig, J., Nijssen, B., Wood, A., Gutmann, E., Mizukami, N., Brekke, L. and Arnold, J.
875 R.: Gridded Ensemble Precipitation and Temperature Estimates for the Contiguous United States, *J. Hydrometeorol.*,
876 16(6), 2481–2500, doi:10.1175/JHM-D-15-0026.1, 2015.
- 877 Newman, A. J., Clark, M. P., Longman, R. J. and Giambelluca, T. W.: Methodological Intercomparisons of Station-
878 Based Gridded Meteorological Products: Utility, Limitations, and Paths Forward, *J. Hydrometeorol.*, 20(3), 531–547,
879 doi:10.1175/JHM-D-18-0114.1, 2019a.
- 880 Newman, A. J., Clark, M. P., Longman, R. J., Gilleland, E., Giambelluca, T. W. and Arnold, J. R.: Use of Daily Station
881 Observations to Produce High-Resolution Gridded Probabilistic Precipitation and Temperature Time Series for the
882 Hawaiian Islands, *J. Hydrometeorol.*, 20(3), 509–529, doi:10.1175/JHM-D-18-0113.1, 2019b.
- 883 Newman, A. J., Clark, M. P., Wood, A. W. and Arnold, J. R.: Probabilistic Spatial Meteorological Estimates for
884 Alaska and the Yukon, *J. Geophys. Res. Atmospheres*, 2020 (under review).
- 885 Papalexiou, S. M.: Unified theory for stochastic modelling of hydroclimatic processes: Preserving marginal
886 distributions, correlation structures, and intermittency, *Adv. Water Resour.*, 115, 234–252, 2018.
- 887 Papalexiou, S. M. and Koutsoyiannis, D.: Battle of extreme value distributions: A global survey on extreme daily
888 rainfall, *Water Resour. Res.*, 49(1), 187–201, doi:10.1029/2012WR012557, 2013.
- 889 Papalexiou, S. M. and Serinaldi, F.: Random Fields Simplified: Preserving Marginal Distributions, Correlations, and
890 Intermittency, With Applications From Rainfall to Humidity, *Water Resour. Res.*, 56(2), e2019WR026331,
891 doi:10.1029/2019WR026331, 2020.
- 892 Parker, W. S.: Reanalyses and Observations: What’s the Difference?, *Bull. Am. Meteorol. Soc.*, 97(9), 1565–1572,
893 doi:10.1175/BAMS-D-14-00226.1, 2016.
- 894 Raftery, A. E., Gneiting, T., Balabdaoui, F. and Polakowski, M.: Using Bayesian Model Averaging to Calibrate
895 Forecast Ensembles, *Mon. Weather Rev.*, 133(5), 1155–1174, doi:10.1175/MWR2906.1, 2005.
- 896 Rodell, M., Beaudoin, H. K., L’Ecuyer, T. S., Olson, W. S., Famiglietti, J. S., Houser, P. R., Adler, R., Bosilovich,
897 M. G., Clayton, C. A., Chambers, D., Clark, E., Fetzer, E. J., Gao, X., Gu, G., Hilburn, K., Huffman, G. J., Lettenmaier,
898 D. P., Liu, W. T., Robertson, F. R., Schlosser, C. A., Sheffield, J. and Wood, E. F.: The Observed State of the Water
899 Cycle in the Early Twenty-First Century, *J. Clim.*, 28(21), 8289–8318, doi:10.1175/JCLI-D-14-00555.1, 2015.
- 900 Scaff, L., Yang, D., Li, Y. and Mekis, E.: Inconsistency in precipitation measurements across the Alaska–Yukon
901 border, *The Cryosphere*, 9(6), 2417–2428, doi:10.5194/tc-9-2417-2015, 2015.
- 902 Schepen, A. and Wang, Q. J.: Model averaging methods to merge operational statistical and dynamic seasonal
903 streamflow forecasts in Australia, *Water Resour. Res.*, 51(3), 1797–1812, doi:10.1002/2014WR016163, 2015.



- 904 Sevruk, B.: International comparison of national precipitation gauges with a reference pit gauge., WMO Instrum. Obs.
905 Methods Rep. No 17, 111, 1984.
- 906 Shen, Y., Zhao, P., Pan, Y. and Yu, J. J.: A high spatiotemporal gauge-satellite merged precipitation analysis over
907 China, *J. Geophys. Res.-Atmospheres*, 119(6), 3063–3075, doi:10.1002/2013jd020686, 2014a.
- 908 Shen, Y., Zhao, P., Pan, Y. and Yu, J.: A high spatiotemporal gauge-satellite merged precipitation analysis over China,
909 *J. Geophys. Res. Atmospheres*, 119(6), 3063–3075, doi:10.1002/2013JD020686, 2014b.
- 910 Shen, Y., Hong, Z., Pan, Y., Yu, J. and Maguire, L.: China’s 1 km Merged Gauge, Radar and Satellite Experimental
911 Precipitation Dataset, *Remote Sens.*, 10(2), 264, doi:10.3390/rs10020264, 2018.
- 912 Sinclair, S. and Pegram, G.: Combining radar and rain gauge rainfall estimates using conditional merging,
913 *Atmospheric Sci. Lett.*, 6(1), 19–22, doi:10.1002/asl.85, 2005.
- 914 Slater, A. G. and Clark, M. P.: Snow Data Assimilation via an Ensemble Kalman Filter, *J. Hydrometeorol.*, 7(3), 478–
915 493, doi:10.1175/JHM505.1, 2006.
- 916 Sun, Q., Miao, C., Duan, Q., Ashouri, H., Sorooshian, S. and Hsu, K.-L.: A Review of Global Precipitation Data Sets:
917 Data Sources, Estimation, and Intercomparisons, *Rev. Geophys.*, doi:10.1002/2017rg000574, 2018.
- 918 Tang, G., Zeng, Z., Long, D., Guo, X., Yong, B., Zhang, W. and Hong, Y.: Statistical and Hydrological Comparisons
919 between TRMM and GPM Level-3 Products over a Midlatitude Basin: Is Day-1 IMERG a Good Successor for TMPA
920 3B42V7?, *J. Hydrometeorol.*, 17(1), 121–137, doi:10.1175/jhm-d-15-0059.1, 2016.
- 921 Tang, G., Behrangi, A., Long, D., Li, C. and Hong, Y.: Accounting for spatiotemporal errors of gauges: A critical step
922 to evaluate gridded precipitation products, *J. Hydrol.*, 559, 294–306, doi:10.1016/j.jhydrol.2018.02.057, 2018a.
- 923 Tang, G., Behrangi, A., Ma, Z., Long, D. and Hong, Y.: Downscaling of ERA-Interim Temperature in the Contiguous
924 United States and Its Implications for Rain–Snow Partitioning, *J. Hydrometeorol.*, 19(7), 1215–1233,
925 doi:10.1175/jhm-d-18-0041.1, 2018b.
- 926 Tang, G., Clark, M. P., Papalexiou, S. M., Newman, A. J., Wood, A. W., Brunet, D. and Whitfield, P. H.: EMDNA:
927 Ensemble Meteorological Dataset for North America [Dataset], FRDR, doi:https://doi.org/10.20383/101.0275, 2020a.
- 928 Tang, G., Clark, M. P., Papalexiou, S. M., Ma, Z. and Hong, Y.: Have satellite precipitation products improved over
929 last two decades? A comprehensive comparison of GPM IMERG with nine satellite and reanalysis datasets, *Remote
930 Sens. Environ.*, 240, 111697, doi:10.1016/j.rse.2020.111697, 2020b.
- 931 Tang, G., Clark, M. P., Newman, A. J., Wood, A. W., Papalexiou, S. M., Vionnet, V. and Whitfield, P. H.: SCDNA:
932 a serially complete precipitation and temperature dataset for North America from 1979 to 2018, *Earth Syst. Sci. Data*,
933 12(4), 2381–2409, doi:https://doi.org/10.5194/essd-12-2381-2020, 2020c.
- 934 Teutschbein, C. and Seibert, J.: Bias correction of regional climate model simulations for hydrological climate-change
935 impact studies: Review and evaluation of different methods, *J. Hydrol.*, 456–457, 12–29,
936 doi:10.1016/j.jhydrol.2012.05.052, 2012.
- 937 Trenberth, K. E., Dai, A., Rasmussen, R. M. and Parsons, D. B.: The Changing Character of Precipitation, *Bull. Am.
938 Meteorol. Soc.*, 84(9), 1205–1218, doi:10.1175/BAMS-84-9-1205, 2003.
- 939 Vila, D. A., de Goncalves, L. G. G., Toll, D. L. and Rozante, J. R.: Statistical Evaluation of Combined Daily Gauge
940 Observations and Rainfall Satellite Estimates over Continental South America, *J. Hydrometeorol.*, 10(2), 533–543,
941 doi:10.1175/2008JHM1048.1, 2009.



- 942 Weedon, G. P., Balsamo, G., Bellouin, N., Gomes, S., Best, M. J. and Viterbo, P.: The WFDEI meteorological forcing
943 data set: WATCH Forcing Data methodology applied to ERA-Interim reanalysis data, *Water Resour Res.*, 50(9), 7505–
944 7514, doi:10.1002/2014wr015638, 2014.
- 945 Willkofer, F., Schmid, F.-J., Komischke, H., Korck, J., Braun, M. and Ludwig, R.: The impact of bias correcting
946 regional climate model results on hydrological indicators for Bavarian catchments, *J. Hydrol. Reg. Stud.*, 19, 25–41,
947 doi:10.1016/j.ejrh.2018.06.010, 2018.
- 948 Wood, A. W., Leung, L. R., Sridhar, V. and Lettenmaier, D. P.: Hydrologic Implications of Dynamical and Statistical
949 Approaches to Downscaling Climate Model Outputs, *Clim. Change*, 62(1), 189–216,
950 doi:10.1023/B:CLIM.0000013685.99609.9e, 2004.
- 951 Wu, H., Adler, R. F., Tian, Y., Huffman, G. J., Li, H. and Wang, J.: Real-time global flood estimation using satellite-
952 based precipitation and a coupled land surface and routing model, *Water Resour. Res.*, 50(3), 2693–2717,
953 doi:10.1002/2013wr014710, 2014.
- 954 Xie, P. and Xiong, A.-Y.: A conceptual model for constructing high-resolution gauge-satellite merged precipitation
955 analyses, *J. Geophys. Res. Atmospheres*, 116(D21), doi:10.1029/2011JD016118, 2011.
- 956 Xu, S., Wu, C., Wang, L., Gonsamo, A., Shen, Y. and Niu, Z.: A new satellite-based monthly precipitation
957 downscaling algorithm with non-stationary relationship between precipitation and land surface characteristics, *Remote
958 Sens. Environ.*, 162, 119–140, doi:10.1016/j.rse.2015.02.024, 2015.
- 959 Yamazaki, D., Ikeshima, D., Tawatari, R., Yamaguchi, T., O’Loughlin, F., Neal, J. C., Sampson, C. C., Kanae, S. and
960 Bates, P. D.: A high-accuracy map of global terrain elevations, *Geophys. Res. Lett.*, 44(11), 5844–5853,
961 doi:10.1002/2017GL072874, 2017.
- 962 Yang, D., Goodison, B. E., Ishida, S. and Benson, C. S.: Adjustment of daily precipitation data at 10 climate stations
963 in Alaska: Application of World Meteorological Organization intercomparison results, *Water Resour. Res.*, 34(2),
964 241–256, doi:10.1029/97WR02681, 1998.
- 965 Yang, D., Kane, D., Zhang, Z., Legates, D. and Goodison, B.: Bias corrections of long-term (1973-2004) daily
966 precipitation data over the northern regions, *Geophys. Res. Lett.*, 32(19), n/a-n/a, doi:10.1029/2005gl024057, 2005.
- 967 Yin, J., Gentile, P., Zhou, S., Sullivan, S. C., Wang, R., Zhang, Y. and Guo, S.: Large increase in global storm runoff
968 extremes driven by climate and anthropogenic changes, *Nat. Commun.*, 9(1), 4389, doi:10.1038/s41467-018-06765-
969 2, 2018.
- 970